DYNAMIC PERFORMANCE OF OFFSET-PRELOADED TWO PAD FOIL BEARINGS

by

SHRIKANT ASHOK YADAV

Presented to the Faculty of the Graduate School of

The University of Texas at Arlington in Partial Fulfillment

of the Requirements

for the Degree of

MASTER OF SCIENCE IN MECHANICAL ENGINEERING

THE UNIVERSITY OF TEXAS AT ARLINGTON

DECEMBER 2012

Acknowledgements

I sincerely thank my committee chair, Dr. Daejong Kim for his guidance, and support throughout the course of research. I would also like to thank Dr. Kent Lawrence and Dr. Bo Wang for serving as committee member.

I would like to express my gratitude to Kermit Beird and Sam Williams from machine shop for helping me at each stage in fabrication and assembly of test setup. I would like to thank my colleagues and friends in Microturbomachinary and Energy Systems Lab for their help and support. I would also like to acknowledge the financial support provided by Dr. Kim and sponsor.

And last but not the least, I would thank my family and friends for their love and support for all these years.

December 14, 2012

Abstract

DYNAMIC PERFORMANCE OF OFFSET-PRELOADED TWO PAD FOIL BEARINGS

Shrikant Ashok Yadav, MS
The University of Texas at Arlington, 2012

Supervising Professor: Daejong Kim

Commercial application of the air foil bearing (AFB) in microturbomachinary have been acknowledged. Absence of external pressurizing and lubricating system makes them light and compact. Simple construction, low friction drag and reliability at high speed operations are few more advantages of the AFBs. With all these advantages AFB proves to be the suitable option for oil-free small turbomachinery which includes micro gas turbines with shaft power less than 1000hp. Micro gas turbine generators are typically two shaft configuration with power generation capacity less than 500KW. Although many micro gas turbines with AFBs have been developed, due to the proprietary nature of their bearings, no specific information about shape and configuration of the bearings is available.

This work presents the dynamic performance of offset-preloaded two pad foil bearings, which is designed and developed for the sponsor project. The scope of the sponsor project was to design journal bearings and thrust bearings for 12KW gas turbine operating at rated engine speed of 138,000 rpm. At this high speed operation, rotor stability is an important issue. From the previous research, it is known that bearings with multi pad configurations are more stable than single pad configuration. Hence, an offset-preloaded two pad bearing configuration was selected for further developed for the sponsor project. Dynamic performance of the bearing was investigated by calculating

frequency-dependent stiffness coefficients and damping coefficients. And the stability analysis for cylindrical mode was performed by determining modal impedances; where positive modal damping over all frequency is interpreted as a stable rotor-bearing system. A code developed by Dr. Kim, which implements the perturbation method for evaluating the frequency-dependent force coefficients is used for this purpose. The geometric and operational parameters are the input for this code. The bump stiffness and structural damping loss factor of the bump foil was evaluated from load-deflection tests, which were used as input parameter to the simulation.

In addition to original designed orientation, dynamic performance of the bearing was evaluated for various clocked orientations like +/- 90^{o} and +/- 45^{o}. Results indicated that at all the clocked orientations, the bearing is stable. Hence, unlike single pad circular foil bearings, this offset-preloaded two pad bearing is stable at any clocked orientation. This novel feature of the offset-preloaded two pad bearing makes it possible to install the bearing in any orientation.

Table of Contents

Acknowledgements iii

Abstract iv

List of Illustrations viii

List of Tables x

Nomenclature xi

Chapter 1 Introduction 1

1.1 Air Foil Journal Bearing 1

1.1.1 Principle of Operation: 2

1.2 Air Foil Thrust Bearing 3

1.2.1 Principle of Operation: 3

1.3 Multi-pad Air Foil Bearing 4

1.4 Micro Gas Turbine 5

1.5 Background of Thesis 6

Chapter 2 Literature Review 8

2.1 Research Objective 12

Chapter 3 Configuration and Manufacturing of Foil Bearing 14

3.1 Definition of Clearance 14

3.2 Clearance and Offset Preload in AFB 15

3.3 Manufacturing Process of Foil Bearing 18

3.3.1 Bump Foil 18

3.3.2 Top Foil 19

3.3.3 Bearing Sleeve. 21

Chapter 4 Gas Film Lubrication Theory 23

4.1 Reynolds Equation 24

4.2 Stiffness and Damping Coefficient Equation 24
4.3 Modal Impedance 28
Chapter 5 Results and Discussion 30
5.1 Structural Characterization 30
5.2 Test Setup 32
5.3 Test Results 35
5.4 Clearance and Preload Selection 37
5.5 Effect of Bearing Orientation and Loss Factor 42
Chapter 6 Conclusion and Future Work 51
6.1 Conclusion 51
6.2 Future Work 52
Appendix A Data Acquisition Using Lab View 53
Bibliography 56
Biographical Information 58

List of Illustrations

Figure 1-1 Schematic of Air Foil Journal Bearing 2
Figure 1-2 Air Foil Thrust Bearing, image from [2] 3
Figure 1-3 Multi-pad foil bearing, image from [1] 4
Figure 1-4 Three pad foil bearing with non-uniform bearing clearance, image from [3] 5
Figure 1-5 Rotor configuration for typical single stage micro gas turbine, image from Capstone Turbine Corporation 6
Figure 3-1 Exaggerated Loose Assembly of AFB without Rotor 14
Figure 3-2 Pad angle and offset angle in offset-preloaded two pad bearing [15] 16
Figure 3-3 Hydrodynamic preload in offset-preloaded two pad bearing [15] 16
Figure 3-4 Form-Feed-Hold-Form (a) Forming of bumps (b) Formed bumps are held in holding region of jig 19
Figure 3-5 Bump foils 19
Figure 3-6 Top foil forming jig 1 20
Figure 3-7 Top foil lip forming jig 2 20
Figure 3-8 Top Foil 21
Figure 3-9 Top assembly in Bearing sleeve 21
Figure 3-10 Bearing Sleeve 22
Figure 4-1 Journal bearing in normal operating condition 23
Figure 4-2 Cross section of eccentric journal bearing 28
Figure 5-1 Schematic of load-deflection test without clearance 30
Figure 5-2 Load-deflection test setup top view 32
Figure 5-3 Load-deflection test setup side view 33
Figure 5-4 Proximity curve calibration plot 34
Figure 5-5 Load cell calibration plot 34

Figure 5-6 Load-deflection plot (raw data and curve fitted) 35
Figure 5-7 Load Vs Displacement curve fitted 36
Figure 5-8 Stiffness coefficients with radial clearance 60 μm and preload 49 μm 39
Figure 5-9 Damping coefficients with radial clearance 60 μm and preload 49 μm 39
Figure 5-10 Modal impedance plot for radial clearance 60 μm and preload 49 μm 40
Figure 5-11 Stiffness coefficients with radial clearance 72 μm and preload 46 μm 40
Figure 5-12 Damping coefficients with radial clearance 72 μm and preload 46 μm 41
Figure 5-13 Modal impedance with radial clearance 72 μm and preload 46 μm 41
Figure 5-14 Bearing orientations (a) Original (b) 90^o CCW rotation (c) 90^o CW rotation (d) 45^o CCW rotation (e) 45^o CW rotation 44
Figure 5-15 Stiffness coefficients for original orientation 45
Figure 5-16 Damping coefficients for original orientation 45
Figure 5-17 Stiffness coefficients for 90^o CCW & 90^o CW bearing orientation 46
Figure 5-18 Damping coefficients for 90^o CCW & 90^o CW bearing orientation 46
Figure 5-19 Stiffness coefficients for 45^o CCW bearing orientation 47
Figure 5-20 Damping coefficients for 45^o CCW bearing orientation 47
Figure 5-21 Stiffness coefficients for 45^o CW bearing orientation 48
Figure 5-22 Damping coefficients for 45^o CW bearing orientation 48
Figure 5-23 Impedance plot for original orientation 49
Figure 5-24 Impedance plot for 90^o CCW and 90^o CW orientation 49
Figure 5-25 Impedance plot for 45^o CCW orientation 50
Figure 5-26 Impedance plot for 45^o CW orientation 50
Figure A-0-1 LabVIEW VI Front Panel View 54
Figure A-0-2 LabVIEW VI block diagram 55

List of Tables

Table 3-1 Size and pad configuration for offset-preload two pad bearing 17

Table 3-2 Radial clearance and preload 18

Table 5-1 Stiffness, Energy dissipation and Damping loss factor 37

Table 5-2 Bearing stability with different sets of clearance and preload 42

Nomenclature

x, y, z	Fluid flow Cartesian coordinate defined with x along bearing circumferential direction, y across film thickness, and z along bearing axial direction
u, v, w	Air flow speed within the film
t	Time measured in second
p	Absolute pressure within fluid film
P	Non-dimensionalized pressure
C	Nominal bearing clearance in [m]
h	Local fluid film thickness in [m]
H	Non-dimensionalized film thickness
d	Air foil bearing damping coefficient with first subscript representing direction in cartesian coordinate and second subscript representing bearing response
k	Air foil bearing stiffness coefficient with first subscript representing direction in cartesian coordinate and second subscript representing bearing response
D	Non-dimensionalized damping coefficient with first subscript representing direction in cartesian coordinate and second subscript representing bearing response
K	Non-dimensionalized stiffness coefficient with first subscript representing direction in cartesian coordinate and second subscript representing
$P_{X,Y}$	Perturbed pressure gradient in X and Y direction

P_a	Atmospheric pressure [N / m^2]
R	Bearing Radius [m]
r_p	Preload
τ	Non-dimensionalized time
ω	Rotor speed [rad / s]
ω_s	Excitation frequency [rad / s]
μ	Air dynamic viscosity [$N \cdot s / m^2$]
A_o	Effective bump area covered by a single bump [m^2]
W_o	Reference Load [N]
ν	Frequency ration ω_s / ω
η	Structural damping loss factor

Chapter 1

Introduction

Air foil bearings (AFB) have gained significant attention in recent years because of various advantages. Air being used as a lubricant, eliminates the need for a bulky lubrication system, which is needed for an oil-lubricated bearing. The absence of external pressurizing or lubrication system makes an overall system compact and light weight. Cleaner environment is an additional advantage of using the air as the lubricant. The oil lubricated bearing generally suffers a thermal degradation at a high temperature while the oil becomes too viscous at low temperature. On the contrary, the air foil bearing can operate at wide range of temperature ranging from high temperatures (> 500^{o}C) to cryogenic temperatures [1]. Air foil bearings gained wide acceptance in industry these days, which includes auxiliary power unit, air cycle machine, turbo alternator and small turbomachinery.

1.1 Air Foil Journal Bearing

A schematic of the simple air foil journal bearing is shown in Figure 1-1 . Air foil bearings are made of smooth top foil and one or more complaint corrugated bump foil. When at rest, the top foil supports the rotating journal, and the top foil is supported by bump foil. The bearing center and journal center are slightly offset due to shaft weight or external load; this offset is termed as eccentricity, and is required for initiating the formation of hydrodynamic air film. The surface of the top foil is usually coated with solid lubricants to reduce the start-stop friction. One edge of the bump foil and top foil are welded together on the bearing sleeve to restrain the circular motion of foils while the journal is rotating. Fixed end of top foil is called trailing edge and the free end is called leading edge. The journal rotates from leading edge to trailing edge i.e. free end to fixed end. The underlying corrugated bump foil structure provides a tunable structural stiffness

and coulomb type damping is generated by relative motion between the bump foils and top foils. The structural stiffness of the bump foil is typically controlled by bump geometry and material. Typically super alloy like nickel chromium alloy trademarked as Inconel is used for bump foil and top foil.

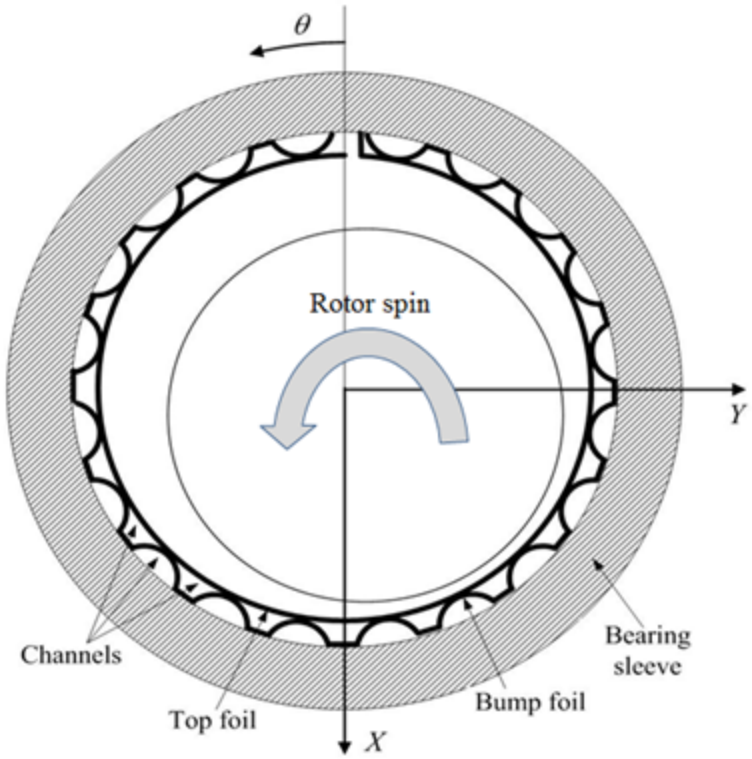

Figure 1-1 Schematic of Air Foil Journal Bearing

1.1.1 Principle of Operation:

Initial radial clearance creates the wedge-shaped void when the journal is at rest. Hydrodynamic pressure starts building up in this void wedge, when the journal starts rotating. Gradually the contact area between journal and top foil is reduced, until the journal reaches lift off speed. Once the lift off speed is reached, journal is completely airborne and solely supported by thin hydrodynamic air film. The underlying compliant structure is self acting in accordance to the change in hydrodynamic pressure. This

inherent ability of self adjusting can accommodate minor thermal growth and centrifugal growth of journal.

1.2 Air Foil Thrust Bearing

Figure 1-2 shows the components of the air foil thrust bearing. Thrust air foil bearing is formed by number of circumferential sections called pad. Each pad consist a pair of bump foil and top foil welded on the backing plate. Similar to journal bearing only one end of bump foil and top foil are welded. The direction of rotation in thrust foil bearing is opposite to that of air foil journal bearing; that is, rotation is from fixed end to free end. The wedge-shaped void in air foil thrust bearing is formed by absence of bump foils at leading edge or fixed end of the top foil. (Exaggerated detail view in Figure 1-2)

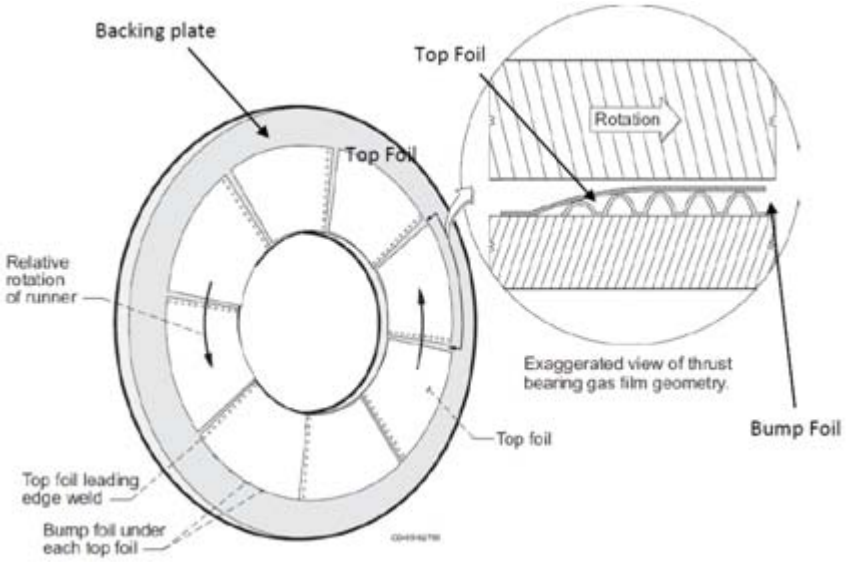

Figure 1-2 Air Foil Thrust Bearing, image from [2]

1.2.1 Principle of Operation:

The principle of operation of air foil thrust bearing is similar to the journal bearing. Thrust foil bearing assembly consists of runner, which rotates between two thrust bearings. At the beginning top foils are in contact with the runner, as the rotor speed

increases, hydrodynamics pressure starts building up, resulting in formation of thin air film.

1.3 Multi-pad Air Foil Bearing

The bearing shown in Figure 1-1 is the single pad bearing. However, this bearing cannot take load at the discontinuity of pad. In contrast, the multi-pad bearing shown in Figure 1-3 can take load in many directions. In both these configurations, single pad and multi-pad configuration, the radial clearance between top foil and rotor is uniform along the circumferential direction if the bearing is lightly loaded. This uniform bearing clearance leads the rotor to the instability at higher speeds. In order to avoid rotor instability, it is important to have a bearing configuration with non uniform radial clearance. Figure 1-4 shows the three-pad bearing with non uniform bearing clearance along circumference. From the figure it can seen that the bearing center and top foil center are not concentric, this amount of offset is termed as hydrodynamic offset which is discussed in detail in section 3.2.

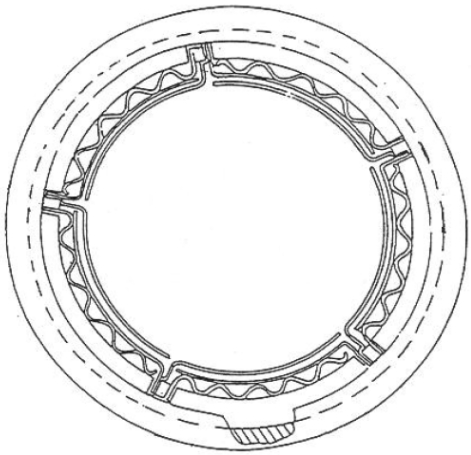

Figure 1-3 Multi-pad foil bearing, image from [1]

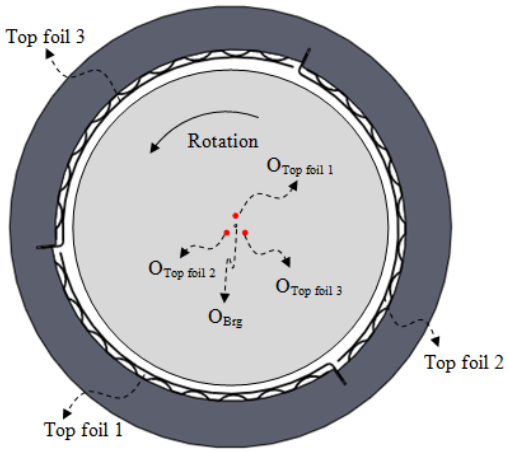

Figure 1-4 Three pad foil bearing with non-uniform bearing clearance, image from [3]

1.4 Micro Gas Turbine

Because AFBs use air as lubricating fluid, they are light and compact, AFBs are perfectly suitable for micro gas turbines with shaft power ranges below 1000hp. Several commercial micro gas turbines with AFBs have been developed in recent years. Capstone Turbine Corporation (www.capstoneturbine.com)have developed C30, C60 and C200 family of the engines using AFBs. C30 is the smallest engine with 31.75 mm shaft diameter, operating at 116000 rpm generating 30 KW of electric power. The rotor for all these engines has four radial AFBs and one double acting air foil thrust bearing. The thrust bearing for C200 is located in front of compressor, while for C30 and C60 thrust bearing is located between the compressor and turbine. Due to proprietary nature of their bearings, detail design and bearing structure are not known.

All the foil bearing supported micro gas turbine rotors typically use a two rotor design with the two rotors being connected through a flexible coupling. Figure 1-5 shows a general rotor configuration for the micro gas turbine with single stage compressor and

turbine. The small solid shaft connecting the gas generator rotor and alternator rotor is the flexible coupling and also sometimes called a quill shaft.

Figure 1-5 Rotor configuration for typical single stage micro gas turbine, image from Capstone Turbine Corporation

1.5 Background of Thesis

This thesis is derived from a recent industry-sponsored project developing 12kW micro gas turbine generators for remote cell phone towers. The gas turbine generator is oil-free and the generator rotor configuration is two-shaft system similar to Figure 1-5. Details of the rotor configuration are not provided here due to confidentiality issue with the sponsor. Rated engine speed is 138,000 rpm with maximum over speed of 154,000 rpm. The rotor shaft is a solid construction with 21 mm in diameter (bearing diameter is also 21 mm) with compressor and turbine impellers attached to both ends of the shaft.

The sponsor project scope was to design radial and thrust foil bearings and prototype manufacturing to meet the design specification of the sponsor. First step in any bearing design is to find the bearing load, and it was found from the force and moment balance of the shaft. Critical speed analysis was done for the project, but the results are not included in this thesis due to sponsor request. Thermal issue is another important

design factor to be considered in the bearing design. Due to high speed operation, lot of heat is generated in the bearing itself. In addition, heat conducted from the combustion chamber and turbine impeller to the bearings and rotor also needs to be taken care of through appropriate cooling system around the bearing. All these heat sources cause thermal expansion of rotor and also bearing. When rotor thermal expansion far exceeds that of bearing, bearing loses all the required clearance, hence leading to thermal runaway and bearing seizure. A proper thermal management strategy should allow similar thermal expansion of both shaft and bearing, and also cooling air flow through the bearings should be minimized to allow better system efficiency. Comprehensive thermal analysis was performed for entire bearing and engine housing during the project period, and a thermal gradient of 75^{o} C between bearing and sleeve was predicted.

At high speed operations, rotor stability is another important issue. Preliminary analysis showed that the single pad foil bearings are not stable at design speed. In order to tackle the rotor stability issue, an offset-preloaded two pad foil bearing configuration with an existing bump design was adopted for the sponsor project.

Overall scope of the thesis is to measure stiffness and damping characteristics of the existing bumps when they are used for the chosen two pad foil bearing and to find design clearance and hydrodynamic preload (to be explained later) for the rotor to be stable at design speed. More rigorous stability analysis including conical mode and various external disturbances including impeller aerodynamic forces and non-linear effect of gas film is on-going work in the project team. .

Chapter 2

Literature Review

This section presents the previous research and advancements in air foil bearings. Extensive research has been carried out to study the effect of important parameters such as load capacity, radial clearance, and thermal characteristics on gas bearing performance. Heshmat et al [4] were first to present the hydrodynamic analysis of foil bearings. They coupled the Reynolds equation with structural model of foils to consider compliant bump foil structure in the static performance of foil thrust bearing.

Load capacity of foil bearing is the maximum constant load that can be supported by the bearing operating with constant speed and steady state condition [5]. DellaCorte and Valco [5] developed a rule of thumb for estimating the load capacity of the foil bearing. Asperity contact and local friction was observed when the nominal clearance approached the average roughness of the shaft and top foil surfaces. Taking this into consideration and using the data available from previous experiments, the empirical relationship was formulated.

Iordanoff [6] developed the analytical formula for evaluation of bump foil stiffness for free end and clamped end. The analysis included the friction between top foil and bump foil, sleeve and bump foil, and coupling forces between the adjacent bumps.

Radial clearance of the air foil bearing is important design characteristic affecting the performance of the bearing. In contrast to the oil lubricated bearing, gas lubricated bearings have very small radial clearance. However, foil bearing clearance is not visible due to non-conformance of bump foil and top foil with the bearing sleeve and shaft [7]. Due to this reason, the radial clearance of AFB is measured by performing load deflection test. The load-deflection test is performed with a test bearing assembled on to a rigid shaft firmly fixed to stationary structure, and push-pull loading is applied against the

bearing to measure load-deflection curve of the bearing. Once the curve for load deflection test is obtained, the boundary of null bearing stiffness marks the amount of diametric clearance of the foil bearing. Radil et al [7] conducted the load capacity test on bearings with different radial clearance measured using the above mentioned load-deflection test. The test foil bearing floating on rotating shaft was loaded until the dramatic change was observed in friction torque, this change in torque denoting the rubbing contact and hence the maximum load capacity. It was observed that each test bearing has optimum radial clearance with maximum load capacity. However, bearing with insufficient clearance exhibited lower load capacity due to premature thermal runaway. On the contrary, bearing with radial clearance twice the optimum suffered only 20% reduction in load capacity.

The compliant surface in foil bearing provides the tunable structural stiffness and coulomb type damping. Heshmat et al [8] measured the bump foil stiffness and observed that the bump foil stiffness depends on bump material, bump pitch and bump height. Furthermore, San Andres et al. [9] investigated the difference in the structural stiffness with different clearance. Load deflection curve was recorded for three different bearing clearances: large clearance, zero clearance, and negative clearance (interference). It was recorded that structural stiffness varied with the initial preload at low loads, while at high load all three bearing exhibited the same structural stiffness.

Extensive, analytical and experimental research has been carried out to improve the load capacity and stability of the air foil bearing. All the analytical studies performed earlier assumed uniform bump stiffness distribution. To study the effect of variation of the bump stiffness on load capacity and bearing performance, Kim [10] conducted a parametric study on static and dynamic performance of foil bearing under variation of bump stiffness and bearing geometry. Two geometric configurations were studied along

with stiffness variation in each sub configuration. Circular bearing with one continuous bump foil and top foil and another bearing made with three sets of bump foils and top foils. Furthermore each configuration had variable stiffness, with stiffness variation in axial direction for first configuration and in circumferential direction for second configuration. Average film thickness of 3 microns at the heavily loaded region was used as criteria to record the maximum load capacity. From the load capacity analyses it was recorded that stiffness variation had insignificant effect on the load capacity of the bearing. On the contrary it was observed that geometric variation of bearing clearance had significant effect on the load capacity, with significant drop in the load capacity for three pad bearing. To investigate the dynamic performance of the bearing, frequency-dependent bearing stiffness and damping coefficients was calculated using perturbation method. The bump stiffness variation showed insignificant effect on force coefficients. However, in comparison with single bump foil bearing, significant reduction in cross coupled stiffness was recorded in the three pad foil bearing. Furthermore, stability analyses of the single foil bearing and three pad bearing was conducted using time domain orbit simulation. Higher onset speed of instability for the three pad bearing was recorded, indicating better stability as compared to the single pad bearing.

Along with the bump foil, many other compliant structures for air foil bearings are studied by researchers. Kim [11] introduced a new type of compliant structure by replacing the bump foil with axially stretched compression spring. Analytical and experimental studies were conducted to determine load capacity, structural stiffness and damping coefficients of the bearing. In addition, a new method of cooling was introduced and cooling effectiveness was studied by testing bearing at 20000 rpm with and without cooling.

Metal mesh material is another alternative compliant structure studied by researchers. Metal mesh foil bearing consists of top foil resting on the metal mesh pad. These metal mesh pads are formed by compressing the weave metal wire. Lee et al [12] estimated the linear stiffness coefficient and damping loss factor for the metal mesh foil bearing with three mesh densities of 13.1 %, 23.2 % and 31.6 % .They conducted load deflection test for each configuration at 0 rpm and 30000 rpm. Load deflection curve for loading and unloading cycle was further used to calculate linear stiffness, and damping loss factor was evaluated using area enclosed in hysteresis loop. The results showed highest linear stiffness and damping loss factor for higher mesh density at 0 rpm, and slight decrease in values at 30000 rpm.

Thermal management of air foil bearing (AFB) is another area which has been studied extensively by researchers. In order to get a better insight into heat generation in AFB, Radil et al [13] conducted experiments to determine the temperature profile in AFB. Temperature profile of the bearing was measured using 9 thermocouples arranged in 3 sets on center and edges of the bearing. They conducted tests for speeds ranging from 20,000 to 50,000 rpm and load from 9 to 222 N. The results indicated both journal speed and load increases the bearing temperature with journal speed having the most significant effect.

Kim and Lee [14] developed a 3D thermohydrodynamic model for air foil bearing to predict the temperature of the rotor, bump foil, top foil, bearing sleeve and air film. The channel formed by the region between adjacent bumps and top foil was defined as primary channel and bump foil channel as secondary channel. They modeled these channels as plate fin heat exchanger. Effective heat transfer resistance from top foil to bearing sleeve was measured experimentally and used in model. In addition to this, thermal growth of bump foil, top foil and shaft was also included in the model. Using this

model, further parametric studies were conducted by varying clearance, load, rotor speed and cooling air flow conditions. Their study concluded that rotor temperature increased with decrease in bearing clearance and increased with increase in load and rotor speed. In addition, the thermal expansion of the bump foil and top foil only accounted less than 1 % decrease in the clearance, while the rotor thermal expansion accounts for 20 % decrease in the clearance.

2.1 Research Objective

As discussed in previous section, Kim [10] conducted the parametric studies to investigate the effect of variation of bump stiffness and top foil geometry. The reports indicated that variation of bump stiffness has insignificant effect on bearing characteristics, while the change in top foil geometry (radial clearance) showed significant impact on overall bearing performance. The bearing with continuous top foil exhibited better load capacity as compared to three pad bearing. However, three pad bearing exhibited higher onset speed of instability.

In order to maximize load capacity and to have better rotordynamic performance, an offset-preloaded two pad foil bearing was chosen for the sponsored project; developing 12kW gas turbine generators.

Design parameters of the offset-preloaded two pad bearings are not as simple as the circular single pad foil bearings. Once the bump stiffness is known, clearance, preload, and pivot offset values have to be determined. This thesis presents design study of the bearing in terms of these parameters using experimentally-measured bump stiffness and damping characteristics. Unlike ball bearings, AFBs are custom designed for specific operating conditions including load and its direction. The loading direction decides the orientation of the bearing, hence, the AFB will not perform as predicted if the orientation of the bearing is different from that of the designed orientation. The thesis also

investigates the dynamic characteristics of the designed offset-preloaded two pad bearing under different orientations with respect to the loading direction. Linearized Reynolds equation is used to calculate frequency dependent stiffness coefficients and damping coefficients for the bearing.

.

Chapter 3

Configuration and Manufacturing of Foil Bearing

As discussed in the previous chapter, researchers have carried out extensive analytical and experimental studies to evaluate the effect of bearing parameters on load capacity, force coefficients and stability of bearing. This chapter presents the design considerations and manufacturing process of the offset-preloaded two pad air foil bearings with 21 mm in diameter.

3.1 Definition of Clearance

Air foil bearings have very small clearance ranging in few microns. This leads to the misconception that AFB have mechanical preload without any clearance. Airfoil bearings do have clearance but it is not visible due to looseness of the bump foil and top foil. Figure 3-1 show the assembly of bearing without rotor. As shown in figure, Bump foil is spot welded at only one end and is not in complete confirmation with sleeve curvature and top foil do not completely rest on the bump foil.

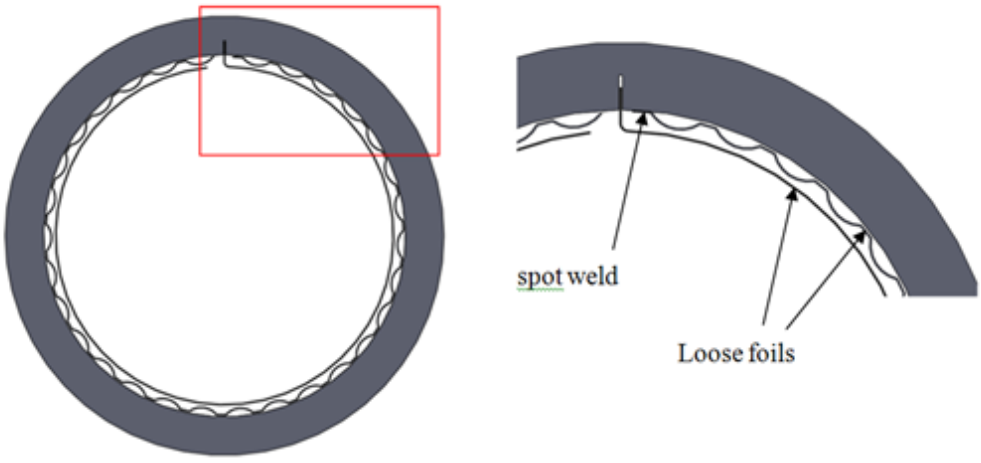

Figure 3-1 Exaggerated Loose Assembly of AFB without Rotor

When the shaft is assembled in the bearing all these loose assemblies make weak contact, which means they can retract even with small pressure, accounting for the cold assembly clearance. This assembly clearance is used for numerical modeling and analyses of AFB. To accurately measure this clearance, NASA engineer suggested using experimental load-deflection curve and identify the cold assembly clearance from soft region of the load-deflection curve. Details of the load-deflection test will be presented later.

3.2 Clearance and Offset Preload in AFB

Parametric study of single pad and three pad bearing conducted by Kim [10] showed that the three pad bearing has higher onset speed of instability. Hence, to avoid the rotor instability at lower speeds it is essential to have non uniform film thickness which can be achieved by multi-pad bearing and offset preload [15]. As shown in Figure 3-2 θ_{pad} is the angular width of the pad and θ_{SB} is angular location of the minimum film thickness. The ratio of these two angles is defined as offset ratio;

$$\gamma = \frac{\theta_{SB}}{\theta_{pad}} \tag{3.1}$$

The film thickness converges from the leading edge to θ_{SB} with minimum at θ_{SB} and diverging after θ_{SB} .As show in Figure 3-3, the bearing center and pad centers are not coincident. This offset distance between O_{Brg} and $O_{Top\,foil\,1}$ can be defined as hydrodynamic preload, r_p .These two parameters, hydrodynamic preload r_p and offset ratio γ are design characteristics of the bearing and are determined based on required bearing performance.

Non-dimensional preload R_p is defined as

$$R_p = \frac{r_p}{C} \tag{3.2}$$

And set bore clearance of the bearing is defined as

$$C_{SB} = C - r_p \tag{3.3}$$

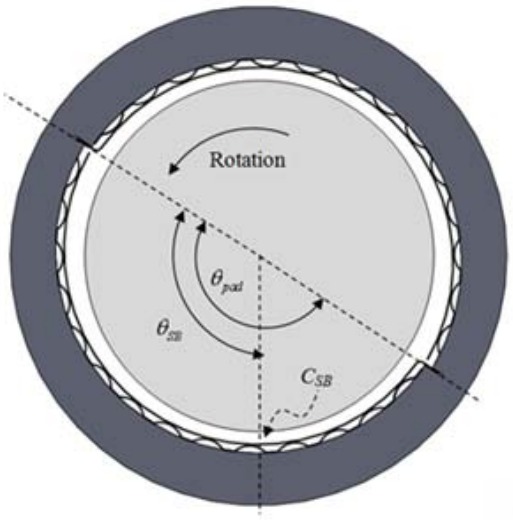

Figure 3-2 Pad angle and offset angle in offset-preloaded two pad bearing [15]

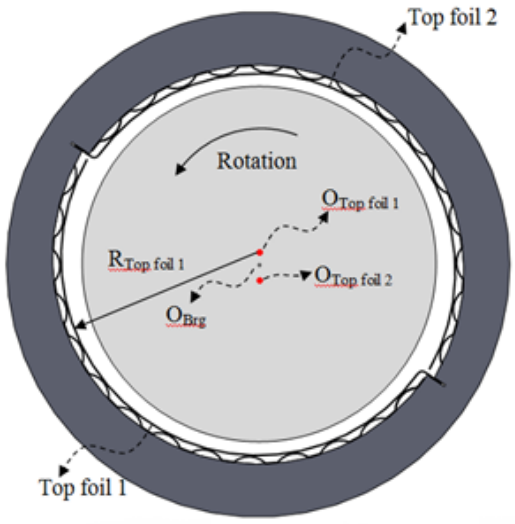

Figure 3-3 Hydrodynamic preload in offset-preloaded two pad bearing [15]

Because centrifugal growth and thermal expansion of the shaft are not negligible, they have to be considered in selecting the foil bearing clearance. When cold assembly clearance is too small, centrifugal growth and thermal expansion of the shaft can lead to thermal runaway and bearing seizure.

Table 3-1 shows the parameters determining overall offset preload configuration explained in Figure 3-2.

Table 3-1 Size and pad configuration for offset-preload two pad bearing

Parameters	Values
Diameter (D)	21mm
Length (L)	21mm
θ_{pad}	178 degree
θ_{SB}	125 degree
$\gamma = \theta_{SB} / \theta_{pad}$	0.7

Due to solid shaft construction, plane stress model of the shaft results in centrifugal expansion of about 2.5 micron in radius. In addition, preliminary thermal analysis of entire engine housing and rotor shaft as mentioned in 1.5 suggests the thermal gradient between the bearing and shaft is about 75^{o}C, which leads to reduction of radial clearance by 8.5 micron. Therefore, total reduction of radial clearance at maximum over speed of 155,000rpm is 11 microns. Therefore, cold assembly radial clearance should be 11 microns larger than normal design clearance at the operating condition. Selection of normal clearance at the operating condition should consider flow Reynolds number and power loss. Power loss is inversely proportional to the clearance but too large clearance can lead to flow turbulence, which in turn leads to the increase of

power loss. Table 3-2 summarizes the range of hydrodynamic preload and clearances that were used in simulations in Chapter 4.

Table 3-2 Radial clearance and preload

ΔC due to centrifugal expansion @ 155,000rpm	- 2.5 μm
Thermal gradient between bearing and sleeve	75°C
ΔC due to thermal gradient @ 155,000rpm	- 8.5 μm
Range of sleeve preload, r_p	40~52 μm (40 43, 46, 49, 52)
Total ΔC	- 11 μm
Cold assembly radial clearance @ 0 rpm	68.5~80.5 μm
Hot assembly radial clearance @ 0 rpm	60~72 μm (60, 63, 66, 69, 72)
Operating radial clearance @ 155,000 rpm	57.5~69.5 μm

3.3 Manufacturing Process of Foil Bearing

Bearing assembly consists of following components:

- Bump Foil
- Top Foil
- Bearing Sleeve

3.3.1 Bump Foil

Bump foil is corrugated compliant structure supporting the top foil. 0.003" thick sheet metal of Nickel-Chromium super alloy trade named Inconel 718 is used for making the bump foils. Two identical bump foils each consisting of 17 bumps is formed by cold forming process. Form-Feed-Hold-Form process is followed for forming the bump foil. As shown in the Figure 3-4 (a), first a plane blank is pressed in the forming jig to form 5 bumps. For forming process 8 tons of pressure is applied using hydraulic press. These

formed bumps are then fed into holding region of the forming jig to constrain the pulling-in of formed bumps into forming region. In order to have uniform bump height distribution it was ensured that each bump passes through middle section of the forming jig.

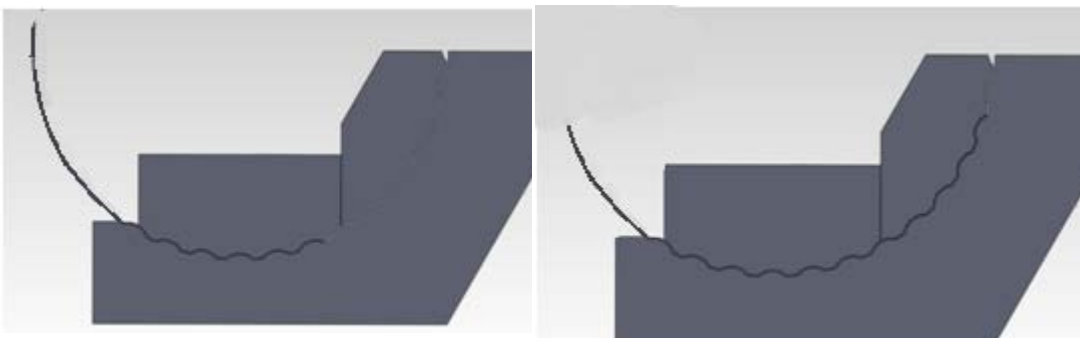

(a) (b)

Figure 3-4 Form-Feed-Hold-Form (a) Forming of bumps (b) Formed bumps are held in holding region of jig

Figure 3-5 Bump foils

3.3.2 Top Foil

Offset-preloaded two pad bearing has two top foils. These two top foils are identical and made of same material as that of bump foils. Each top foil covers the span of 175^{o}. In order to get the desired curvature, the top foil blank is wrapped to a mandrel

having smaller diameter then the required curvature. This mandrel along with wrapped foil is then pressed in the top foil forming jig shown Figure 3-6. A small lip is formed one end of the top foil to ensure easy assembly/disassembly of the top foil in to the bearing sleeve. (Refer Figure 3-9)

Figure 3-6 Top foil forming jig 1

Figure 3-7 Top foil lip forming jig 2

Figure 3-8 Top Foil

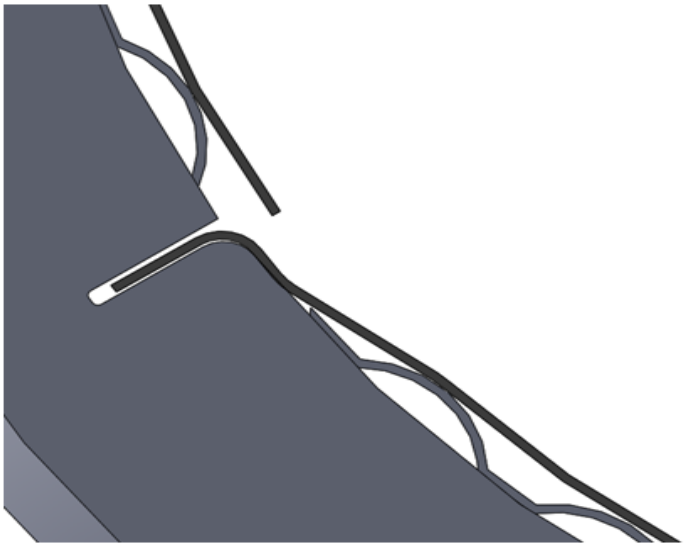

Figure 3-9 Top assembly in Bearing sleeve

Based on the grade of Inconel i.e. 718/750 cold formed bump foil and top foils are heat treated in furnace. Heat treating the foils not only relieves the induced stress but also enhances the tensile properties of the material.

3.3.3 Bearing Sleeve.

Bearing sleeve is made of stainless steel 13-8, and is machined using wire EDM (Electrical Discharge Machining). The offset preload is manufactured into the bearing sleeve. The center of the two curves O1 and O2 are offset by 50 microns each, from the

bearing center and thus the offset preload is created (refer Figure 3-10). The width of the bearing is 21 mm, each curve spans 175^{o} and has slit at the beginning. This slit houses the top foil lip and hence enables easy assembly and disassembly of the top foils.

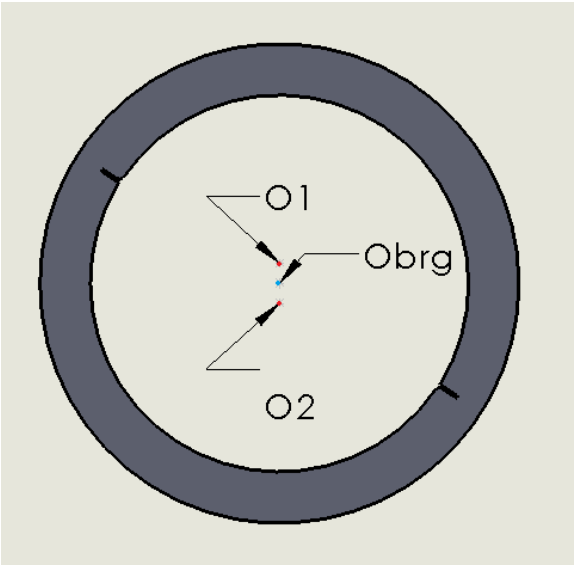

Figure 3-10 Bearing Sleeve

Chapter 4

Gas Film Lubrication Theory

This chapter presents mathematical theory used in the simulation and modal impedance curves presented in Chapter 5. All the theory and formulations presented in this chapter is based on the class notes of ME5390 Applied Tribology taught by Dr. Daejong Kim.

A linearized Reynolds equation is used to calculate frequency-dependent stiffness coefficients and damping coefficients for the bearing. Figure 4-1 shows the schematic of the gas bearing in normal operating condition. Upon rotation of the journal, the gas between the two surfaces of gas bearing is pressurized by wedge and squeeze film effect. This hydrodynamic pressure generated between the surfaces lifts the journal. At steady state, there is no contact between the journal and bearing leading almost zero friction operation.

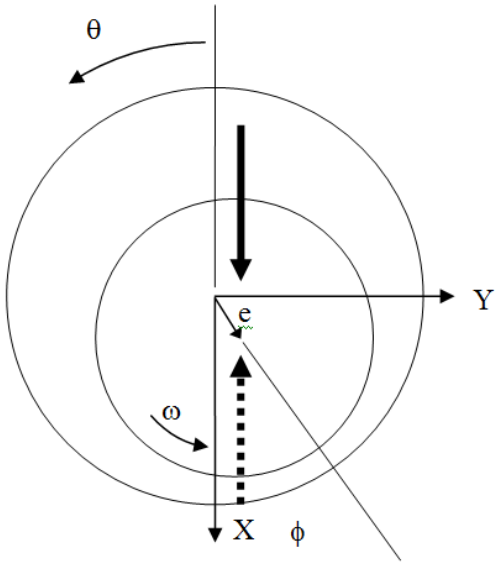

Figure 4-1 Journal bearing in normal operating condition

4.1 Reynolds Equation

Standard governing equation for thin gas film is Reynolds equation developed by Osborne Reynolds in 1886with assumptions of thin gas film, negligible curvature effect and isothermal ideal gas;

$$\frac{\partial}{\partial x}(ph^3\frac{\partial p}{\partial x})+\frac{\partial}{\partial z}(ph^3\frac{\partial p}{\partial z})=6U\mu\frac{\partial}{\partial x}(ph)+12\mu\frac{\partial}{\partial t}(ph) \tag{4.1}$$

4.2 Stiffness and Damping Coefficient Equation

Dynamic performance of the bearing is usually done by calculating the bearing stiffness and damping coefficients. Perturbation method is used to calculate frequency-dependent force coefficients. In perturbation analysis the rotor at static equilibrium e_{X0}, e_{Y0} is given finitely small disturbance of amplitude $\Delta e_x, \Delta e_y$ with excitation frequency ω_s. Once the equilibrium position e_{X0}, e_{Y0} is found, perturbed eccentricity, bump deflection and local thickness is given by following set of equation

$$e_\alpha = e_{\alpha 0} + \Delta e_\alpha e^{i\omega_s t}, \alpha = X, Y \tag{4.2}$$

$$u = u_0 + \Delta u_X e^{i\omega_s t} + \Delta u_Y e^{i\omega_s t} \tag{4.3}$$

$$h = h_0 + \Delta h_X e^{i\omega_s t} + \Delta h_Y e^{i\omega_s t} \tag{4.4}$$

Where

$$h_0 = C + e_{X0}\cos\theta + e_{Y0}\sin\theta + u_0 \tag{4.5}$$

$$\Delta h_X = \Delta e_X \cos\theta + \Delta u_X \tag{4.6}$$

$$\Delta h_Y = \Delta e_Y \sin\theta + \Delta u_Y \tag{4.7}$$

From the perturbed form of film thickness, perturbed pressure is given as

$$p = p_0 + \Delta e_X \, p_X e^{i\omega_s t} + \Delta e_Y \, p_Y e^{i\omega_s t} \tag{4.8}$$

For actual numerical analysis, it is easier to use non-dimensionalized equations.

Firstly, Reynolds equation is non-dimensionalized as.

$$\frac{\partial}{\partial\theta}(PH^3\frac{\partial P}{\partial\theta}) + \frac{\partial}{\partial Z}(PH^3\frac{\partial P}{\partial Z}) = \Lambda\frac{\partial}{\partial\theta}(PH) + 2\Lambda\nu\frac{\partial}{\partial\tau_s}(PH) \tag{4.9}$$

where $P = \frac{p}{p_a}$, $H = \frac{h}{C}$, $\varepsilon = \frac{e}{C}$, $\nu = \frac{\omega_s}{\omega}$, $\Lambda = \frac{6\mu\omega}{p_a}\left(\frac{R}{C}\right)^2$ and $\tau_s = \omega_s t$. The perturbed pressure, film thickness, and bump deflections are also non-dimensionalized such as

$$P = P_0 + \Delta P = P_0 + \Delta\varepsilon_X P_X e^{i\tau_S} + \Delta\varepsilon_Y P_Y e^{i\tau_S} \tag{4.10}$$

$$H = H_0 + \Delta H = H_0 + \Delta H_X e^{i\tau_S} + \Delta H_Y e^{i\tau_S} \tag{4.11}$$

$$U = U_0 + \Delta U_X e^{i\tau_S} + \Delta U_Y e^{i\tau_S} \tag{4.12}$$

where $U = \frac{u}{C}$. Inserting non-dimensional form of perturbed pressure, film thickness and bump deflections into non-dimensional Reynolds equation and dropping all the higher terms and rearranging

$$\begin{aligned}
&\frac{\partial}{\partial\theta}\left[P_0{H_0}^3\frac{\partial P_\alpha}{\partial\theta}\right] + \frac{\partial}{\partial Z}\left[P_0{H_0}^3\frac{\partial P_\alpha}{\partial Z}\right] + \\
&\frac{\partial}{\partial\theta}\left[\left(3{H_0}^2P_0H_\alpha + {H_0}^3P_\alpha\right)\left(\frac{\partial P_0}{\partial\theta}\right)\right] + \frac{\partial}{\partial Z}\left[\left(3{H_0}^2P_0H_\alpha + {H_0}^3P_\alpha\right)\left(\frac{\partial P_0}{\partial Z}\right)\right] = \\
&\Lambda\frac{\partial}{\partial\theta}\left(P_0H_\alpha + P_\alpha H_0\right) + 2\Lambda\nu i\left(P_0H_\alpha + P_\alpha H_0\right)
\end{aligned} \tag{4.13}$$

Where

$$H_\alpha \equiv \frac{\Delta H_\alpha}{\Delta \varepsilon_\alpha}, \alpha = X, Y \tag{4.14}$$

Equation for bump dynamics is given as

$$f_b = k_b u + c_b \frac{du}{dt} \tag{4.15}$$

In above equation c_b is equivalent bump viscous damping coefficient calculated using loss factor η and bump stiffness k_b; $c_b = \eta \frac{k_b}{\omega_s}$ Also f_b is bump pressure given as $f_b = pA_o$,substituting all this in equation (4.15) gives

$$pA_0 = k_b u + \eta \frac{k_b}{\omega_s} \frac{du}{dt} \tag{4.16}$$

Non-dimensionalizing above equation gives

$$P = K_b U + C_b \nu \frac{dU}{d\tau_s} = K_b \left(U + \eta \frac{dU}{d\tau_s} \right) \tag{4.17}$$

where $K_b = \frac{k_b C}{p_a A_0}$, $C_b = \frac{\eta k_b C \omega}{p_a A_0 \omega_s} = \frac{\eta}{\nu} K_b$. Inserting equation (4.10) and (4.12) in above equation and canceling zeroth order term.

$$\Delta\varepsilon_X P_X + \Delta\varepsilon_Y P_Y = K_b(1+\eta i)\Delta U_X + K_b(1+\eta i)\Delta U_Y \tag{4.18}$$

Inserting $\Delta U_X = \Delta H_X - \Delta\varepsilon_X \cos\theta$ and $\Delta U_Y = \Delta H_Y - \Delta\varepsilon_Y \sin\theta$ and separating X and Y components.

$$\begin{aligned} \Delta\varepsilon_X P_X &= K_b(1+\eta i)\left(\Delta H_X - \Delta\varepsilon_X \cos\theta\right) \\ \Delta\varepsilon_Y P_Y &= K_b(1+\eta i)\left(\Delta H_Y - \Delta\varepsilon_Y \sin\theta\right) \end{aligned} \tag{4.19}$$

Dividing above equation by $\Delta\varepsilon_\alpha$ gives

$$H_X = \frac{P_X}{K_b(1+\eta i)} + \cos\theta \tag{4.20}$$

$$H_Y = \frac{P_Y}{K_b(1+\eta i)} + \sin\theta \tag{4.21}$$

Inserting equation (4.20) and (4.21) into (4.13) and rearranging

$$\begin{aligned}
&\frac{\partial}{\partial\theta}\left[\Lambda H_0 P_\alpha - P_0 {H_0}^3 \frac{\partial P_\alpha}{\partial\theta}\right] + \frac{\partial}{\partial Z}\left[-P_0 {H_0}^3 \frac{\partial P_\alpha}{\partial Z}\right] \\
&= \frac{\partial}{\partial\theta}\left[{H_0}^3 \frac{\partial P_0}{\partial\theta} P_\alpha - \Lambda P_0\left(\frac{P_\alpha}{K_b(1+\eta i)} + f_\alpha\right) + 3{H_0}^2 P_0\left(\frac{P_\alpha}{K_b(1+\eta i)} + f_\alpha\right)\frac{\partial P_0}{\partial\theta}\right] \\
&+ \frac{\partial}{\partial Z}\left[{H_0}^3 \frac{\partial P_0}{\partial Z} P_\alpha + 3{H_0}^2 P_0\left(\frac{P_\alpha}{K_b(1+\eta i)} + f_\alpha\right)\frac{\partial P_0}{\partial Z}\right] \\
&-2\Lambda\nu i\left(P_0\left(\frac{P_\alpha}{K_b(1+\eta i)} + f_\alpha\right) + P_\alpha H_0\right)
\end{aligned} \tag{4.22}$$

Where $\alpha = X, Y$ and $f_X = \cos\theta,\ f_Y = \sin\theta$

$$\begin{pmatrix} k_{XX} \\ k_{YX} \end{pmatrix} = -\frac{W_0}{C}\frac{R}{2L}\iint \mathrm{Re}(P_X)\begin{pmatrix}\cos\theta \\ \sin\theta\end{pmatrix} d\theta dZ = \frac{W_0}{C}\begin{pmatrix} K_{XX} \\ K_{YX}\end{pmatrix} \tag{4.23}$$

$$\begin{pmatrix} k_{XY} \\ k_{YY} \end{pmatrix} = -\frac{W_0}{C}\frac{R}{2L}\iint \mathrm{Re}(P_Y)\begin{pmatrix}\cos\theta \\ \sin\theta\end{pmatrix} d\theta dZ = \frac{W_0}{C}\begin{pmatrix} K_{XY} \\ K_{YY}\end{pmatrix} \tag{4.24}$$

$$\begin{pmatrix} d_{XX} \\ d_{YX} \end{pmatrix} = -\frac{1}{\omega_s}\frac{W_0}{C}\frac{R}{2L}\iint \mathrm{Im}(P_X)\begin{pmatrix}\cos\theta \\ \sin\theta\end{pmatrix} d\theta dZ = \frac{1}{\omega_s}\frac{W_0}{C}\begin{pmatrix} D_{XX} \\ D_{YX}\end{pmatrix} \tag{4.25}$$

$$\begin{pmatrix} d_{XY} \\ d_{YY} \end{pmatrix} = -\frac{1}{\omega_s}\frac{W_0}{C}\frac{R}{2L}\iint \mathrm{Im}(P_Y)\begin{pmatrix}\cos\theta \\ \sin\theta\end{pmatrix} d\theta dZ = \frac{1}{\omega_s}\frac{W_0}{C}\begin{pmatrix} D_{XY} \\ D_{YY}\end{pmatrix} \tag{4.26}$$

Where $\Delta W_0 = 2P_a RL$

4.3 Modal Impedance

Stability analysis of the bearing is performed by conducting modal analysis of cylindrical mode of rigid rotor. Conical mode shape is out of scope in this thesis due to sponsor request that the rotor geometry (bearing span and moment of inertia) is confidential information.

Equation (4.27) represents the equation of the motion of rotor without external load (refer Figure 4-2).

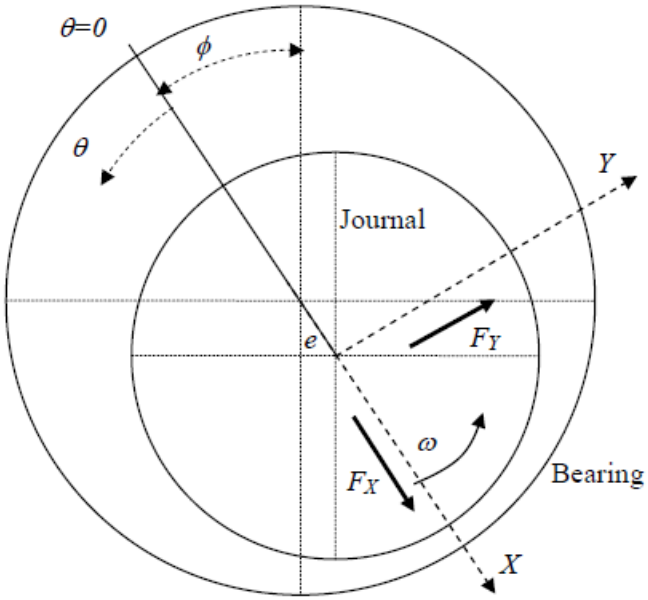

Figure 4-2 Cross section of eccentric journal bearing

$$\begin{aligned} m\ddot{X} + k_{XX}X + k_{XY}Y + d_{XX}\dot{X} + d_{XY}\dot{Y} = 0 \\ m\ddot{Y} + k_{YX}X + k_{YY}Y + d_{YX}\dot{X} + d_{YY}\dot{Y} = 0 \end{aligned} \tag{4.27}$$

Assuming rotor has self sustaining vibration motion with frequency ω_s, such that

$$\begin{Bmatrix} X(t) \\ Y(t) \end{Bmatrix} = \mathrm{Re}\left[\begin{Bmatrix} \delta X \\ \delta Y \end{Bmatrix} e^{j\omega_s t} \right] \tag{4.28}$$

Where Re is real operator and δ_X, δ_Y are phasors with magnitude and phase angle,

Inserting equation (4.28) into (4.27) we get

$$\begin{bmatrix} ms^2 & 0 \\ 0 & ms^2 \end{bmatrix} \begin{Bmatrix} \delta X \\ \delta Y \end{Bmatrix} + \begin{bmatrix} Z_{XX} & Z_{XY} \\ Z_{YX} & X_{YY} \end{bmatrix} \begin{Bmatrix} \delta X \\ \delta Y \end{Bmatrix} = 0 \tag{4.29}$$

Where $s = j\omega_s$ and Z contains both stiffness and damping coefficients,

$$\begin{aligned} Z_{XX} &= K_{XX} + jd_{XX}\omega_s \\ Z_{YX} &= K_{YX} + jd_{YX}\omega_s \\ Z_{XY} &= K_{XY} + jd_{XY}\omega_s \\ Z_{YY} &= K_{YY} + jd_{YY}\omega_s \end{aligned} \tag{4.30}$$

Assuming $Z_K = -ms^2$ and rearranging equation (4.29) we get

$$\begin{bmatrix} Z_{XX} - Z_K & Z_{XY} \\ Z_{YX} & X_{YY} - Z_K \end{bmatrix} \begin{Bmatrix} \delta X \\ \delta Y \end{Bmatrix} = 0 \tag{4.31}$$

In order to have solution for above the 2 X 2 matrix must be zero.

$$\begin{aligned} &(Z_{XX} - Z_K)(Z_{YY} - Z_K) - Z_{XY}Z_{YX} = 0 \\ &{Z_K}^2 - (Z_{XX} + Z_{YY})Z_K + Z_{XX}Z_{YY} - Z_{XY}Z_{YX} = 0 \end{aligned} \tag{4.32}$$

Hence solution for above equation is given by

$$\begin{aligned} Z_1 &= \frac{Z_{XX} + Z_{YY}}{2} + \sqrt{\left(\frac{Z_{XX} + Z_{YY}}{2} \right)^2 - (Z_{XX}Z_{YY} - Z_{XY}Z_{YX})} \\ Z_2 &= \frac{Z_{XX} + Z_{YY}}{2} - \sqrt{\left(\frac{Z_{XX} + Z_{YY}}{2} \right)^2 - (Z_{XX}Z_{YY} - Z_{XY}Z_{YX})} \end{aligned} \tag{4.33}$$

Results of the simulations are presented in 5.4.

Chapter 5

Results and Discussion

5.1 Structural Characterization

From the gas lubrication theory mentioned in the previous chapter, bump foil stiffness and damping loss factor are required to study the dynamic characteristics of AFB. This section explains how the bump stiffness was measured.

In order to evaluate the structural bump stiffness, the load deflection test was conducted using a 21mm shaft and a circular AFB (using the same bump foils in the actual two pad foil bearing) sized for a zero clearance between shaft and the bearing. Figure 5-1 shows the relative displacement of the shaft with respect to the bearing when assembly clearance is zero. The overlapped region represents the amount of bump deflection in the foil bearing. Due to non-zero clearance, the contact angle between the shaft and bearing is always 90^{o}.

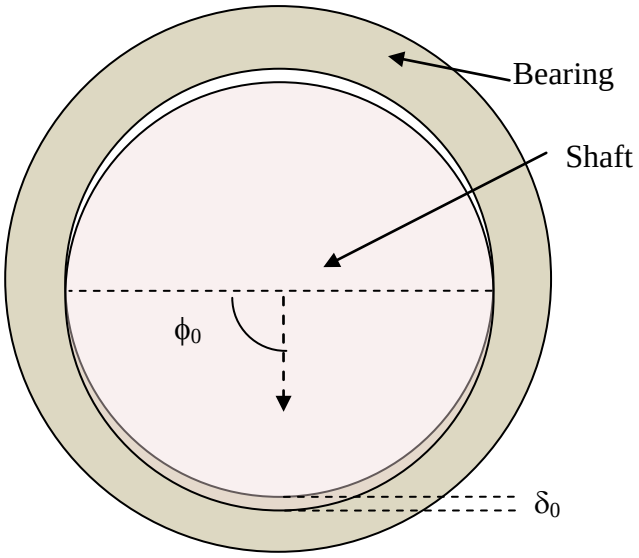

Figure 5-1 Schematic of load-deflection test without clearance

When the rotor moves δ_0 beyond the contact with the bearing surface, local bump deflection is expressed as

$$\delta(\phi) = \delta_0 \cos\phi \quad (-\phi_0 < \phi < \phi_0) \tag{5.1}$$

where ϕ_0 = 90 degree. Local bump reaction force in radial direction is given as

$$f(\phi) = \hat{k}_{bump}\delta(\phi) \tag{5.2}$$

Where, $\hat{k}_{bump}$ is the bump stiffness per unit circumferential angle. If bump pitch is *p* and radius of the bearing sleeve is R_{sleeve},

$$\hat{k}_{bump} = k_{bump}\frac{R_{sleeve}}{p} \tag{5.3}$$

Bump reaction force in the vertical direction is a cosine component of the radial reaction force;

$$f_{Vertical}(\phi) = f(\phi)\cos\phi = \hat{k}_{bump}\delta(\phi)\cos\phi = \hat{k}_{bump}\delta_0\cos^2\phi \tag{5.4}$$

Total vertical reaction force from the contacting bumps is the summation of (5.4) over $-\phi_0 < \phi < \phi_0$;

$$\begin{aligned} F_{Vertical} &= 2\int_0^{\phi_0}\hat{k}_{bump}\delta_0\cos^2\phi d\phi = 2\hat{k}_{bump}\delta_0\int_0^{\phi_0}\cos^2\phi d\phi \\ &= \hat{k}_{bump}\delta_0\int_0^{\phi_0}(1+\cos 2\phi)d\phi = k_{bump}\frac{R_{sleeve}}{p}\delta_0\left(\phi_0 + \frac{\sin 2\phi_0}{2}\right) \end{aligned} \tag{5.5}$$

Total structural stiffness is defined as local gradient of the force;

$$k_{structural} = \frac{\partial F_{Vertical}}{\partial \delta_0} = k_{bump}\frac{R_{sleeve}}{p}\left(\phi_0 + \frac{\sin 2\phi_0}{2}\right) \tag{5.6}$$

The $k_{structural}$ of the bump foil was evaluated experimentally and using equation (5.6) k_{bump} was calculated. This k_{bump} was further used for stiffness and damping coefficient evaluations and modal analysis of bearing.

5.2 Test Setup

Figure 5-2 shows the test setup designed and manufactured to perform load-deflection tests. A bearing sleeve with bump foils and top foils is mounted on stationary shaft. This shaft is then mounted on a pair of V-block and is held in place. Push-pull mechanism is connected to bearing sleeve through the load cell. Description of the instruments for load-deflection is as followings. The shaft is mounted on a pair of V-block, which can accommodate shafts having different diameters. A load cell measures actual load applied to the bearing, and it is located between the test bearing and push-pull loading mechanism. The push-pull mechanism consists of long screw rotating in a fixed pedestal and a piston cylinder arrangement which converts rotating motion of screw into linear motion.

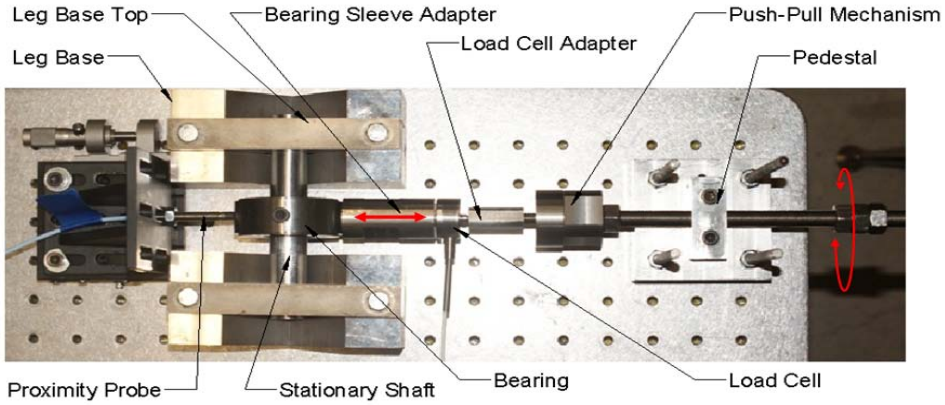

Figure 5-2 Load-deflection test setup top view

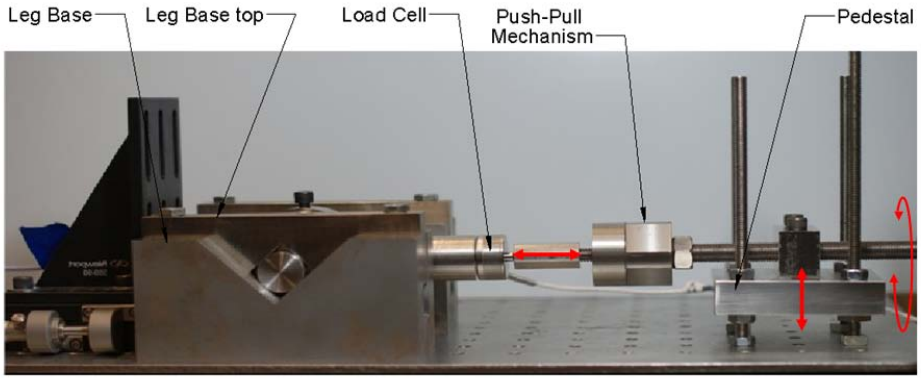

Figure 5-3 Load-deflection test setup side view

An inductive type proximity probe is used to measure the displacement of the bearing sleeve. The inductive type probe being sensitive to surface material, it is important to calibrate the proximity probe before use. A Linear stage with a least count of 1 μm was used for calibration. A DC output voltage of the probe is measured for displacement of 50 μm .Figure 5-4 shows the calibration curve for the proximity probe. Note that the nonlinear region below 200 μm is neglected.

The load cell is a strain gauge type, which needs a bridge circuit for its operation, which is provided by DMD 465 bridge sensor. Additionally, DMD 465 bridge sensor also amplifies the load cell output voltage.DMD 465 bridge sensor and LCFD 25 load cell were calibrated using known weights, the plot for which is show in Figure 5-5.

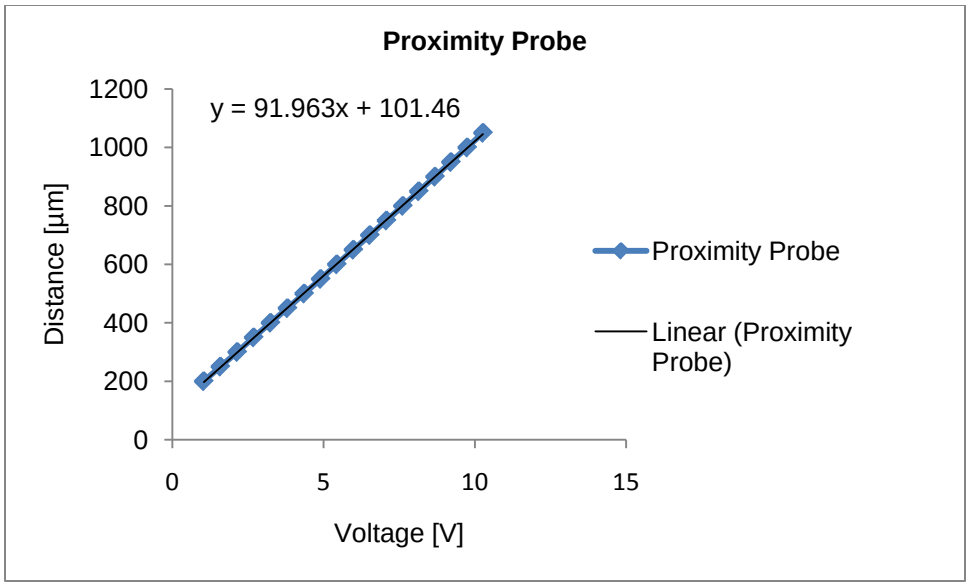

Figure 5-4 Proximity curve calibration plot

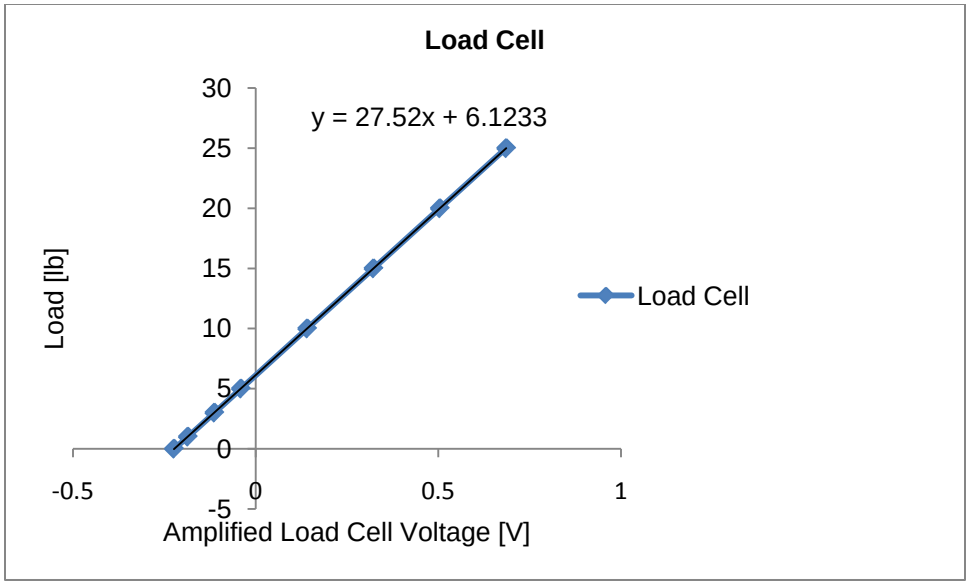

Figure 5-5 Load cell calibration plot

5.3 Test Results

The structural stiffness of the bearing was evaluated by calculating slope of the load-deflection plot for the bearing. Figure 5-6 shows the plot of load-deflection test including raw data and curve fitted plot. The curve fits use sixth order polynomial equations to accurately follow the raw data curves.

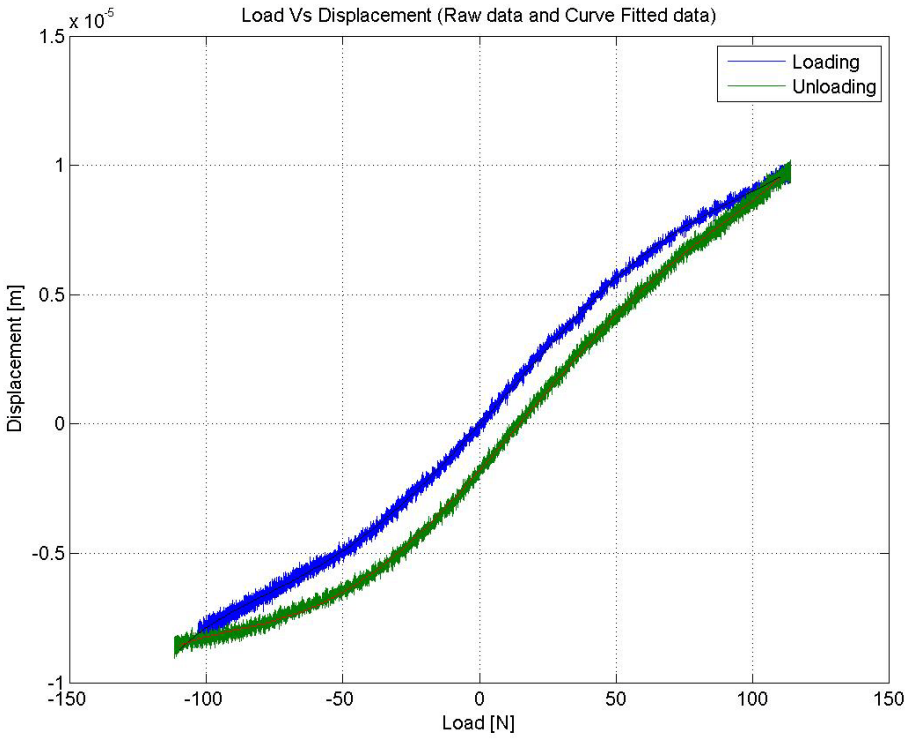

Figure 5-6 Load-deflection plot (raw data and curve fitted)

Figure 5-7 show the curve fitted plot along with the points between which the slope of the curve is plotted. The loading and unloading cycle shows the strong nonlinear behavior of the AFB. The stiffness of the bearing varies nonlinearly from low loads to high loads. The region at the low loads shows lower value of stiffness, defined as soft region. The large stiffness at high load is evident from the higher values of slopes and this effect is termed as hardening. Additionally, the loading and unloading cycle follow different path

indicating hysteresis. This hysteresis behavior of the AFB provides the damping ability to the bearing.

A simple model of a mechanical system with structural damping (or dry-friction) can be used to represent the hysteresis. The area enclosed by the curves denotes the energy dissipation ΔW . A damping loss factor from the model is

$$\eta = \frac{\Delta W}{\pi k X^2} \tag{5.7}$$

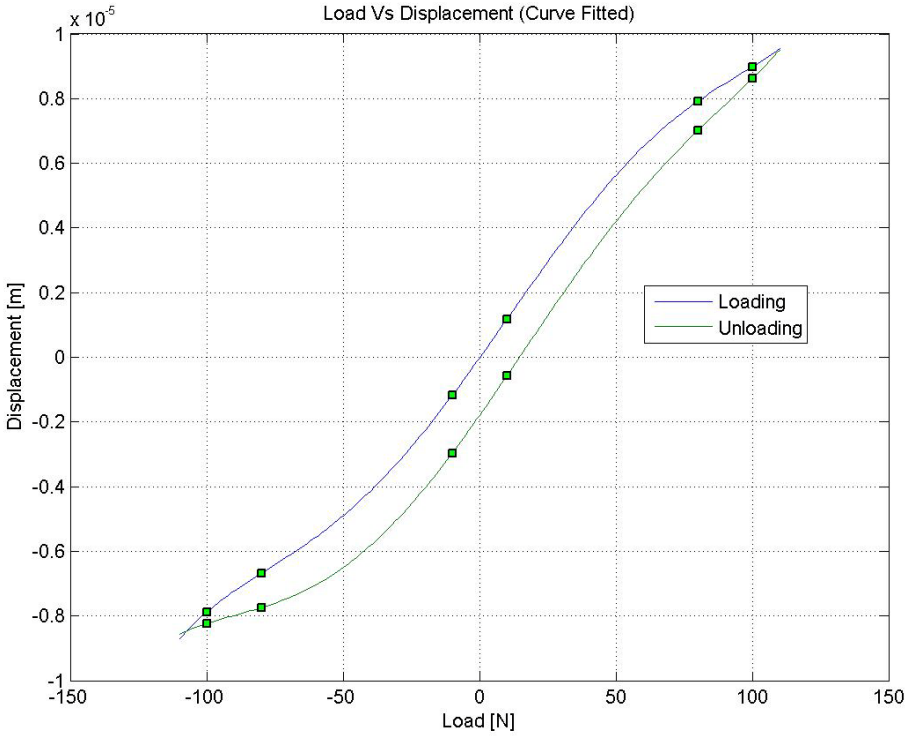

Figure 5-7 Load Vs Displacement curve fitted

Table 5-1 shows the stiffness between two marked points in Figure 5-7 and damping loss factor. Three different sets of load-deflection tests were carried out on the bearing. The averaged stiffness value of the bearing was calculated from the soft region which was further used for evaluating the single bump stiffness using equation (5.6).

From average bearing structural stiffness, individual bump stiffness was estimated as k_{bump}=8.95e5 N/m for sleeve radius of 11mm and bump pitch of 1.85mm. Additionally, structural damping loss factor η was calculated using equation (5.7) and their average value is 0.134.

Table 5-1 Stiffness, Energy dissipation and Damping loss factor

	Area Enclosed in Loop[N-m]	$k_{structural}$ in Soft Region [N/m]		$k_{structural}$ After Hardening [N/m]		Damping Loss Factor η
		Loading	Unloading	Loading	Unloading	
1	0.00027707	8.52E+06	8.38E+06	1.87E+07	1.67E+07	1.28E-01
2	0.00020995	8.05E+06	8.52E+06	1.87E+07	1.67E+07	1.02E-01
3	0.00035398	8.04E+06	8.10E+06	2.39E+07	1.81E+07	1.73E-01

5.4 Clearance and Preload Selection

Clearance and preload selection is the most important part of AFB design. As discussed in the literature review, clearance selection affects heat generation in bearing and thus the overall bearing performance. Bearing with optimum radial clearance have maximum load capacity and exhibits better dynamic performance.

Dynamic performance and stability analysis was conducted using perturbation method. A code developed by Dr. Kim uses geometrical and operational parameters of the bearing to calculate bearings dynamic coefficients. Furthermore, it also calculates the modal impedances, important for studying stability analysis. The bump stiffness k_{bump} , which is one of the input parameter for simulation is 8.95e5N/m. The average value of damping loss factor η equal to 0.134 from Table 5-1 was used. From equation (4.23)-(4.26) it is evident, that the dynamic coefficients are frequency-dependent. Hence, the simulation was performed by varying $\nu = \omega_s / \omega$ from 0.05 to 3. Additionally, the set of simulations with different values of radial clearances (here hot assembly clearance in

Table 3-2 was used as reference) and preloads were simulated. The radial clearance was varied from 60 μm to 72 μm and preload was varied from 40 μm to 52 μm with an increment of 3 μm.

Figure 5-8 ~ Figure 5-10 shows the plot for stiffness coefficients, damping coefficients and modal impedance for radial clearance 60 μm and preload 49 μm. From the stiffness and damping plots it is evident that the bearing has higher direct coefficients and lower cross-coupled coefficients, indicating that the bearing is stable. Furthermore, the absence of negative imaginary impedance or unstable eigenmode confirms the bearing stability.

Figure 5-11~Figure 5-13 shows the plot for stiffness coefficients, damping coefficients and modal impedance for radial clearance 72 μm and preload 46 μm. Although, in this case the direct coefficients are higher than the cross-coupled coefficients they are lower than the previous case. Also from the modal impedance this bearing has unstable eigenmode at V below around 0.3. Hence the bearing with this combination of clearance and preload is susceptible to instability.

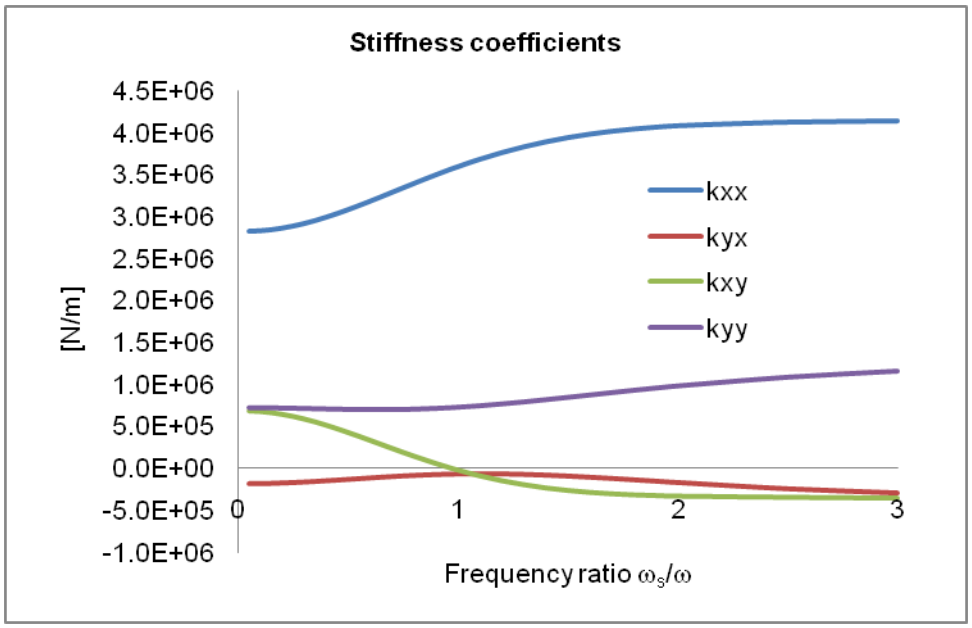

Figure 5-8 Stiffness coefficients with radial clearance 60 μm and preload 49 μm

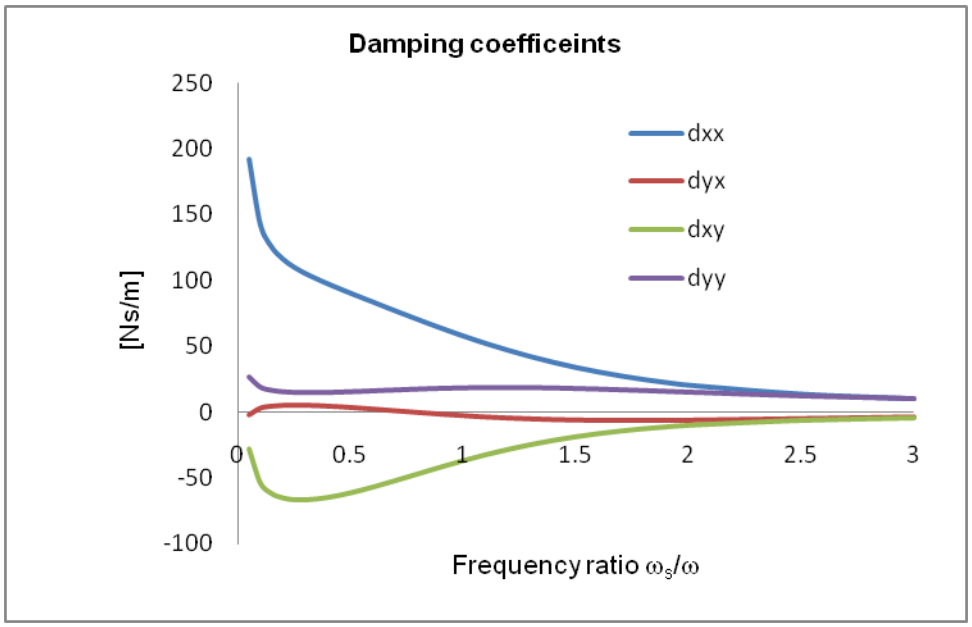

Figure 5-9 Damping coefficients with radial clearance 60 μm and preload 49 μm

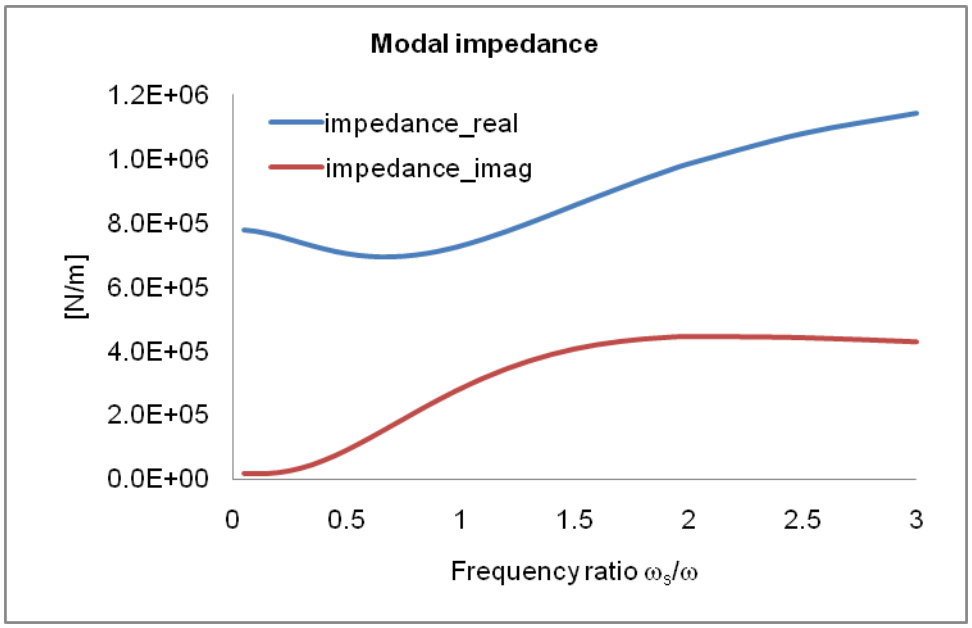

Figure 5-10 Modal impedance plot for radial clearance 60 μm and preload 49 μm

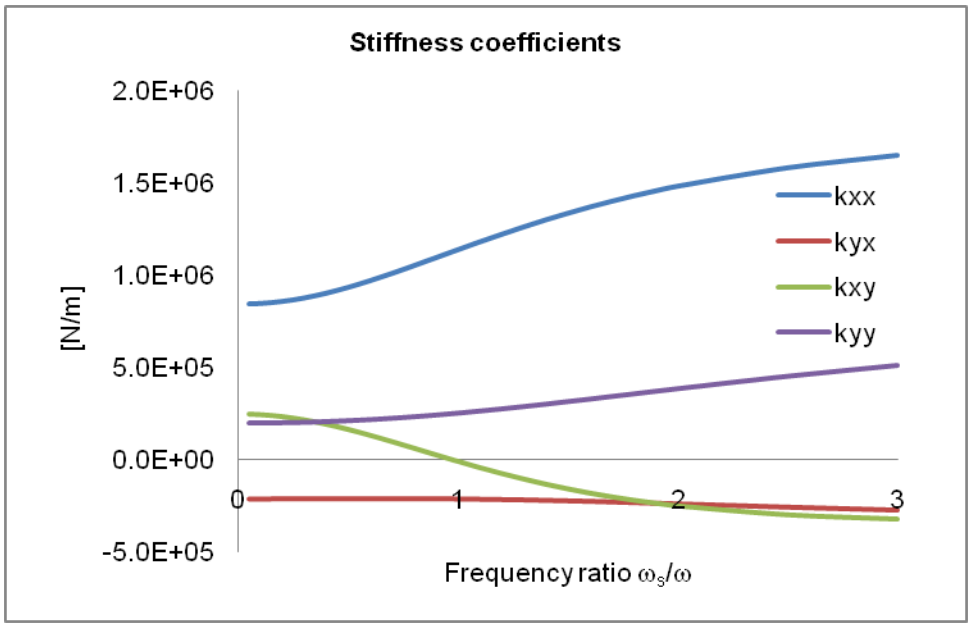

Figure 5-11 Stiffness coefficients with radial clearance 72 μm and preload 46 μm

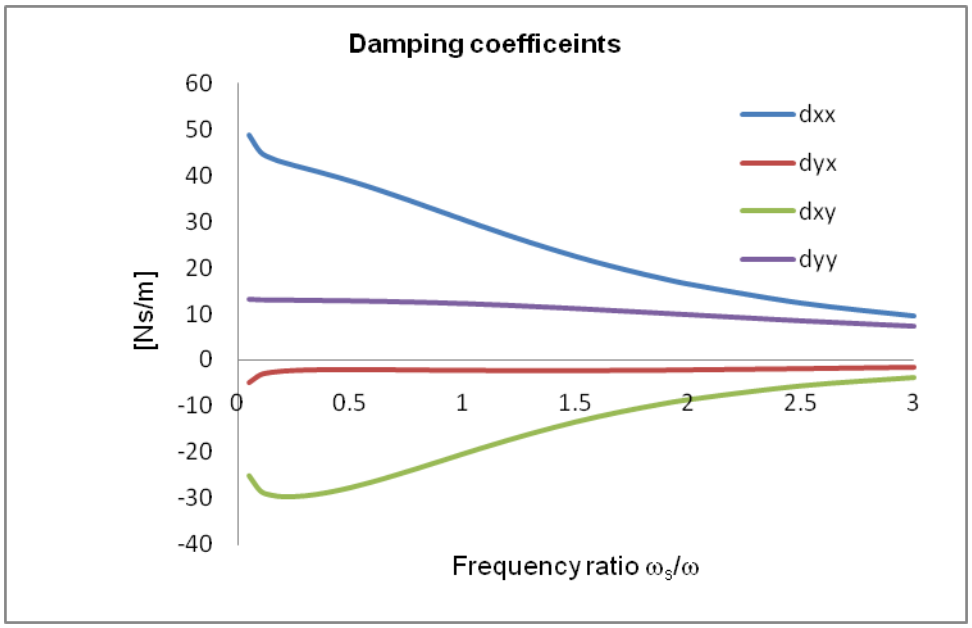

Figure 5-12 Damping coefficients with radial clearance 72 μm and preload 46 μm

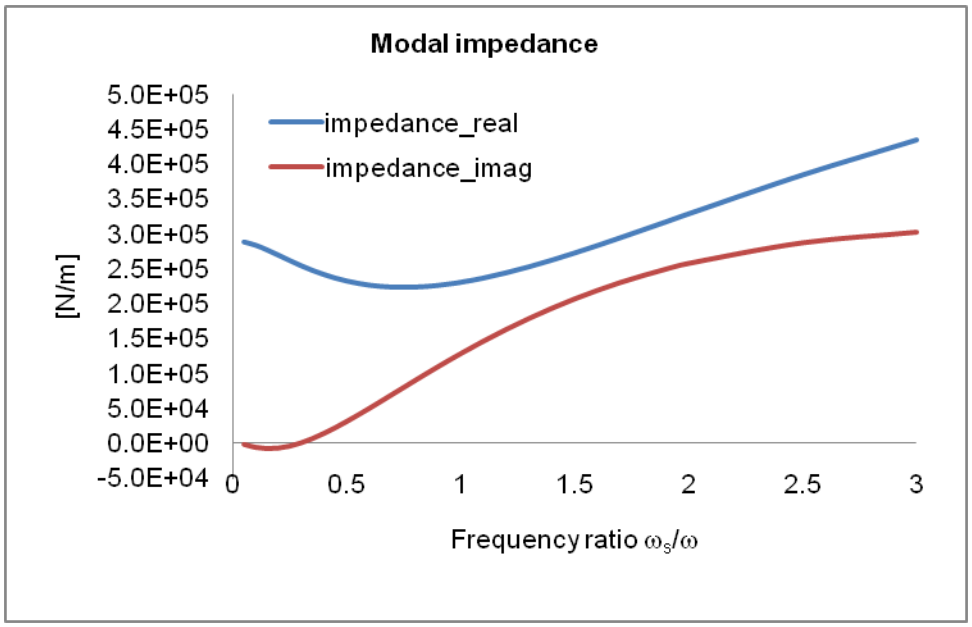

Figure 5-13 Modal impedance with radial clearance 72 μm and preload 46 μm

Table 5-2 shows the simulation results for the various combinations of clearance and preload. The number in each cell denotes the ratio of preload and clearance while the cell color denotes stability. The cell with the green color indicates that given combination is stable and red color indicates instability.

Table 5-2 indicates that the bearing is stable around 49 μm of preload with the hot assembly clearance ranging from 60 μm to 72 μm. Hence the preload of 50 μm and hot assembly clearance of 63 μm was selected as the design preload and clearance.

Table 5-2 Bearing stability with different sets of clearance and preload

		Hot assembly clearance [μm]				
		60	63	66	69	72
Preload [μm]	40	0.666667	0.634921	0.606061	0.57971	0.555556
	43	0.716667	0.68254	0.651515	0.623188	0.597222
	46	0.766667	0.730159	0.69697	0.666667	0.638889
	49	0.816667	0.777778	0.742424	0.710145	0.680556
	52	0.866667	0.825397	0.787879	0.753623	0.722222

5.5 Effect of Bearing Orientation and Loss Factor

In order to study the effect of change in bearing orientation on the bearing performance, simulation was performed by clocking the orientation of bearing in different angles. This was done by varying the pad start angle. Figure 5-14 shows the original orientation and clocked orientations, which were simulated. All the simulation were performed with preload of 50 μm and hot assembly clearance of 63 μm with structural damping loss factor η value as 0.134.

Figure 5-15~Figure 5-16 shows the stiffness and damping coefficient of the original orientation at 155,000 rpm with frequency ratio ranging from 0.05 to 3. The direct stiffness and damping coefficients are higher, while all the cross-coupled terms are lower

than direct terms. Furthermore, the stability analysis renders that the bearing is completely stable and does not have any unstable eigenmodes (refer Figure 5-23). Figure 5-17~Figure 5-18 represents the stiffness and damping coefficients for 90^o clockwise (CW) and 90^o counter-clockwise (CCW) orientations. The stiffness and damping coefficient for the 90^o CW and 90^o CCW are identical. While as compared to the original bearing, k_{xx} for original orientation is equal to k_{yy} for 90^o CW and 90^o CCW orientations, indicating higher stiffness in the horizontal direction. Also the cross coupled stiffness and damping coefficient have opposite signs as compared to original orientation. Figure 5-19~Figure 5-22 are the plots for dynamic coefficients for bearing rotation in 45^o CCW and 45^o CW orientations. The direct stiffness's for 45^o CW and 45^o CCW orientations shows similar trend as shown by 90^o CW and 90^o CCW orientations, but the value of direct stiffness's in 45^o CW and 45^o CCW orientations are lower as compared to original orientation. Additionally, the stability analysis for all five orientations have identical impedance plot (refer Figure 5-23~Figure 5-26), Indicating that the bearing is stable and has no unstable eigenmodes, irrespective of orientation of the bearing. The reason for the identical impedance plots is that, this bearing only support rotor weight and is lightly loaded. So in all the orientations the rotor eccentricities are very small. Due to small eccentricities the rotor is stable in all orientations, which is the unique feature of offset-preloaded two pad bearing.

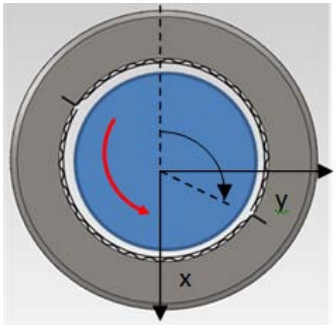

(a)

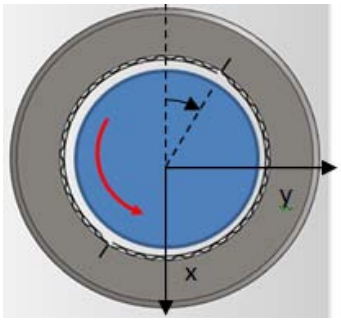

(b)

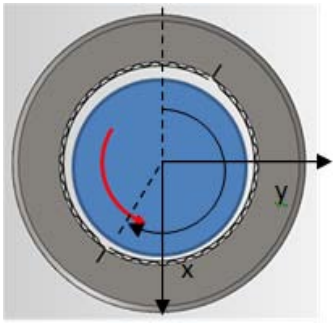

(c)

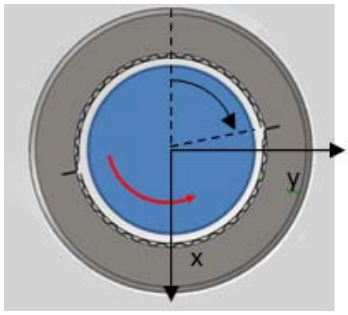

(d)

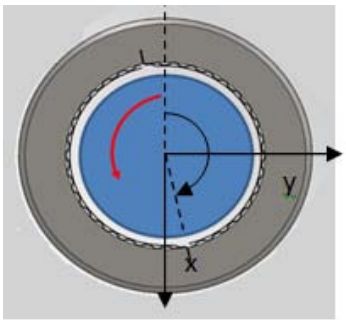

(e)

Figure 5-14 Bearing orientations (a) Original (b) 90^{o} CCW rotation (c) 90^{o} CW rotation (d) 45^{o} CCW rotation (e) 45^{o} CW rotation

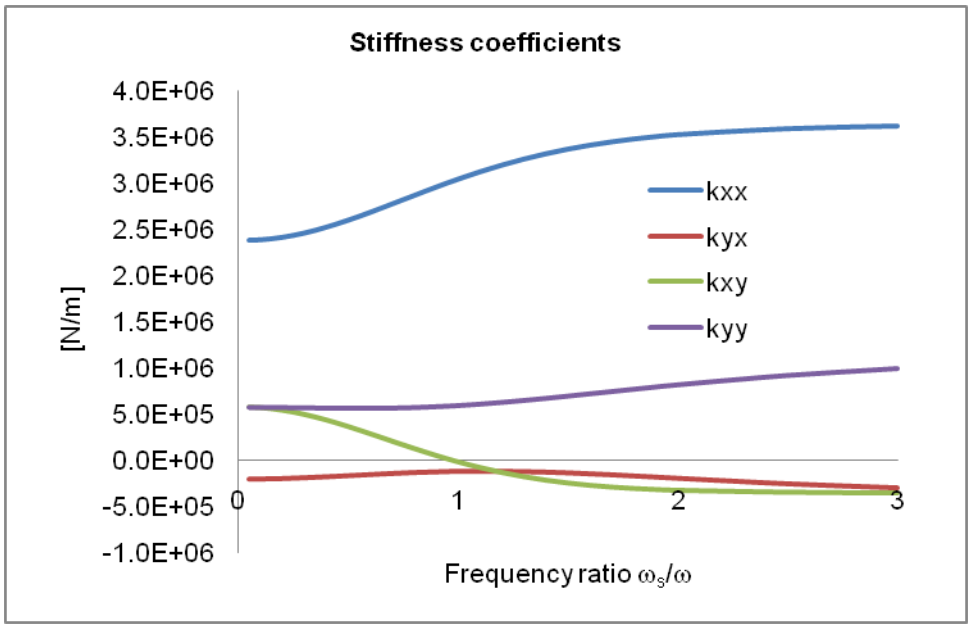

Figure 5-15 Stiffness coefficients for original orientation

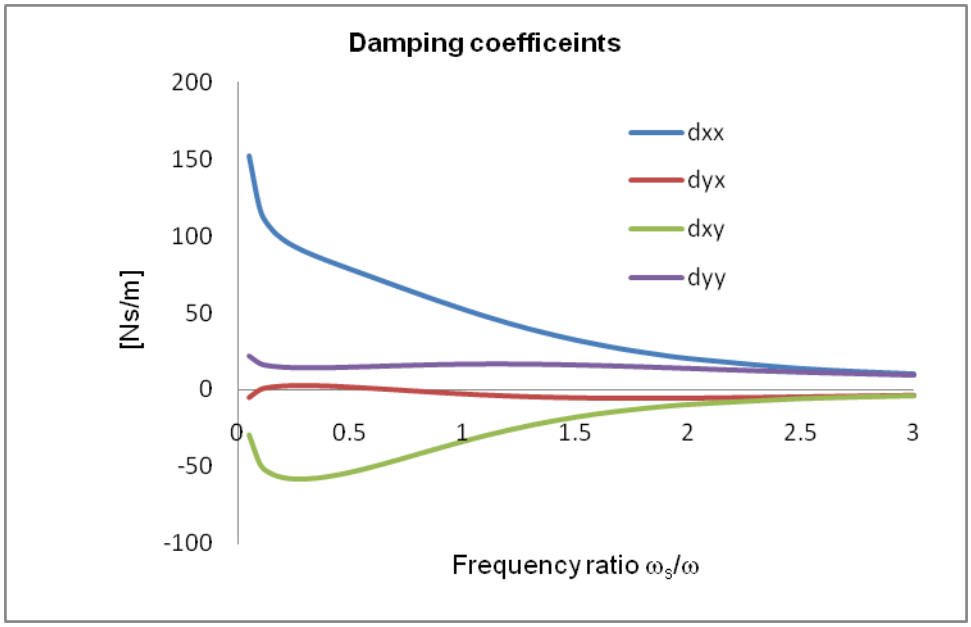

Figure 5-16 Damping coefficients for original orientation

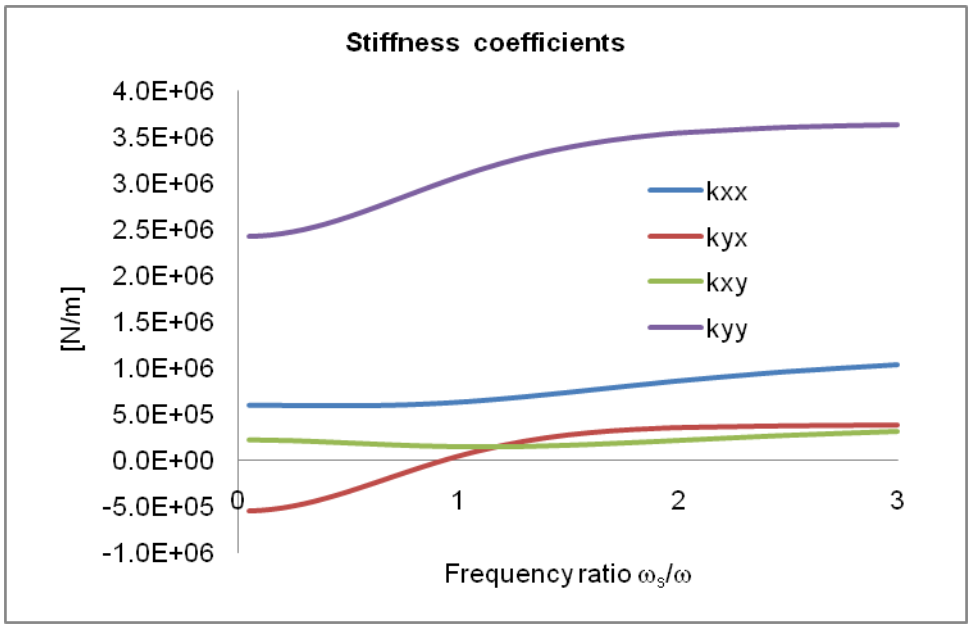

Figure 5-17 Stiffness coefficients for 90^{o} CCW & 90^{o} CW bearing orientation

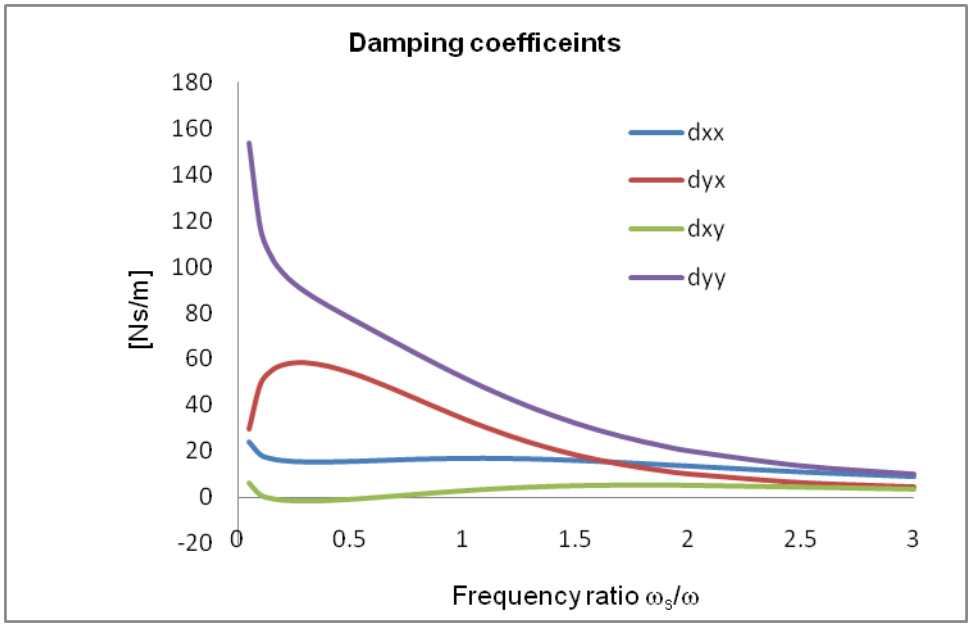

Figure 5-18 Damping coefficients for 90^{o} CCW & 90^{o} CW bearing orientation

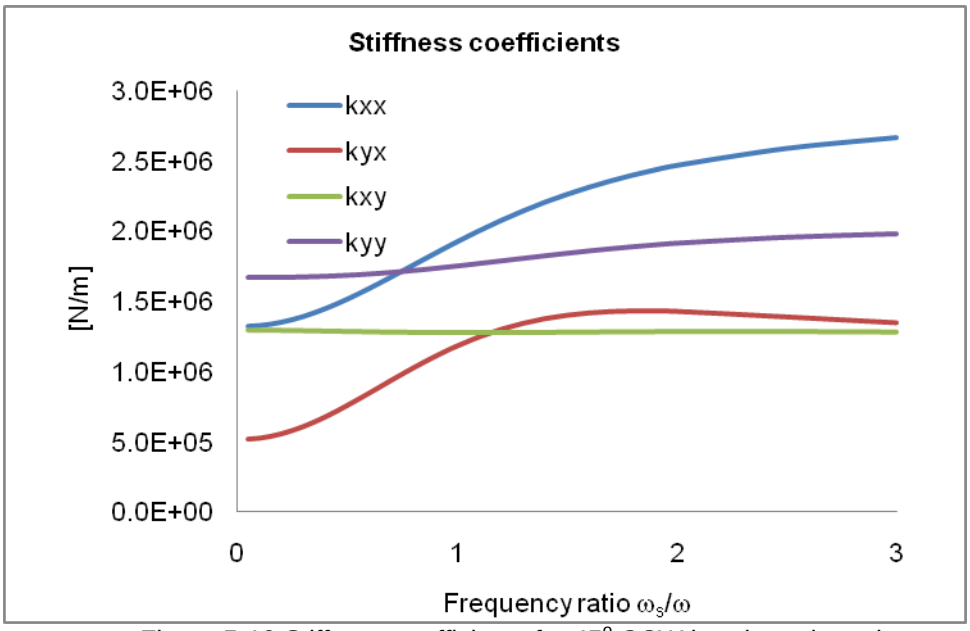

Figure 5-19 Stiffness coefficients for 45° CCW bearing orientation

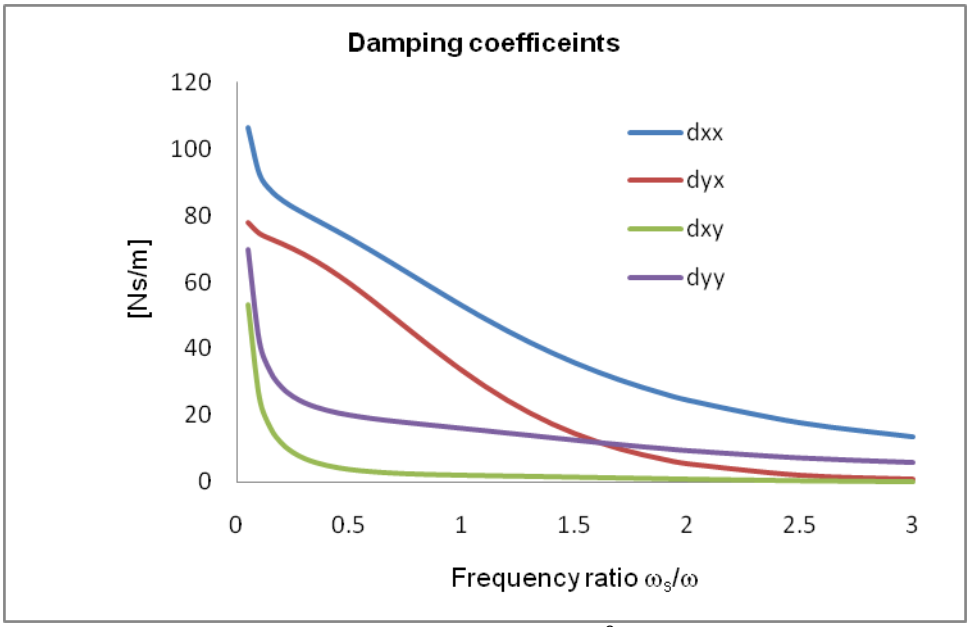

Figure 5-20 Damping coefficients for 45° CCW bearing orientation

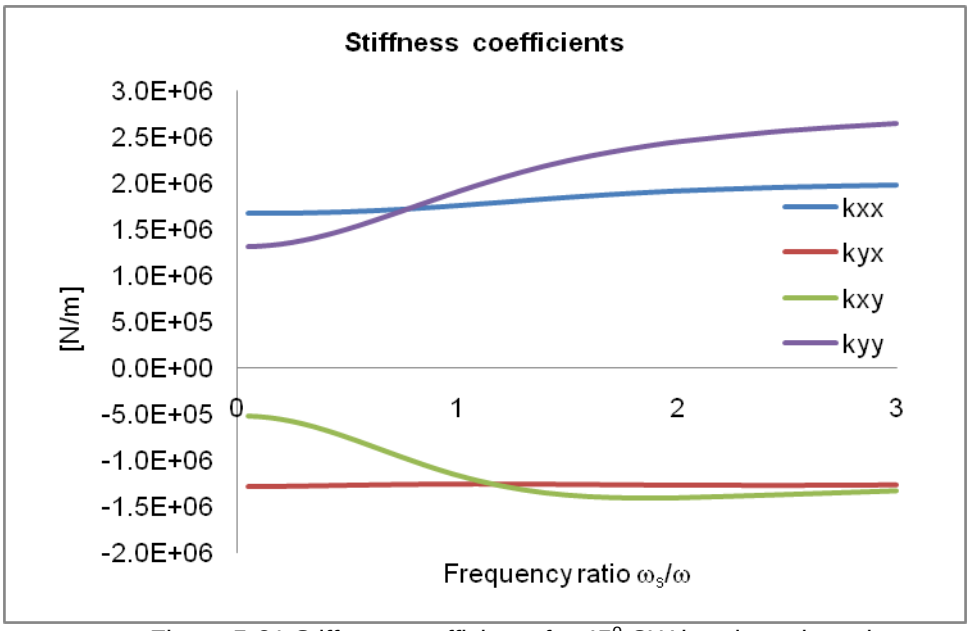

Figure 5-21 Stiffness coefficients for 45° CW bearing orientation

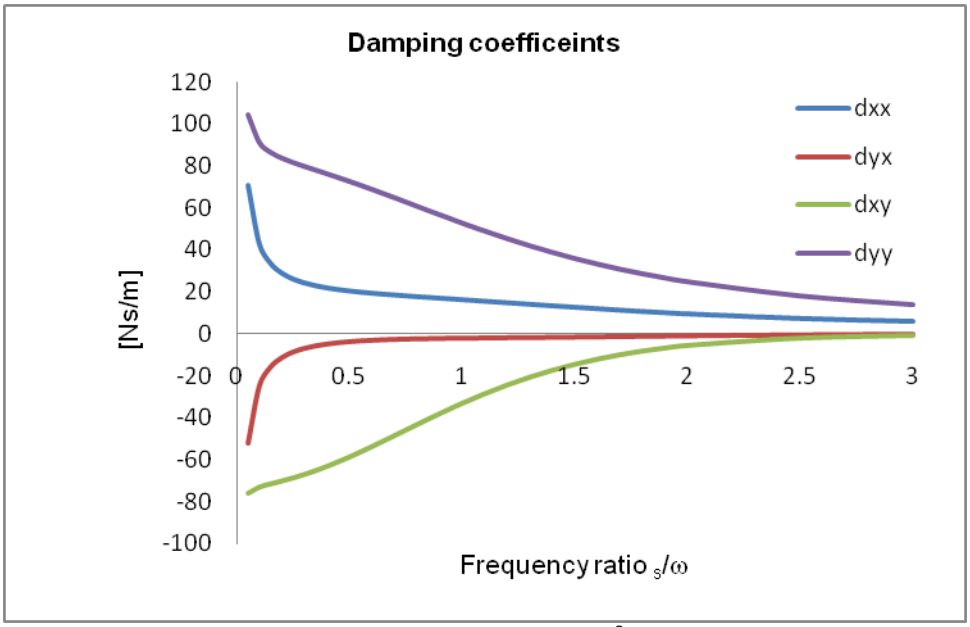

Figure 5-22 Damping coefficients for 45° CW bearing orientation

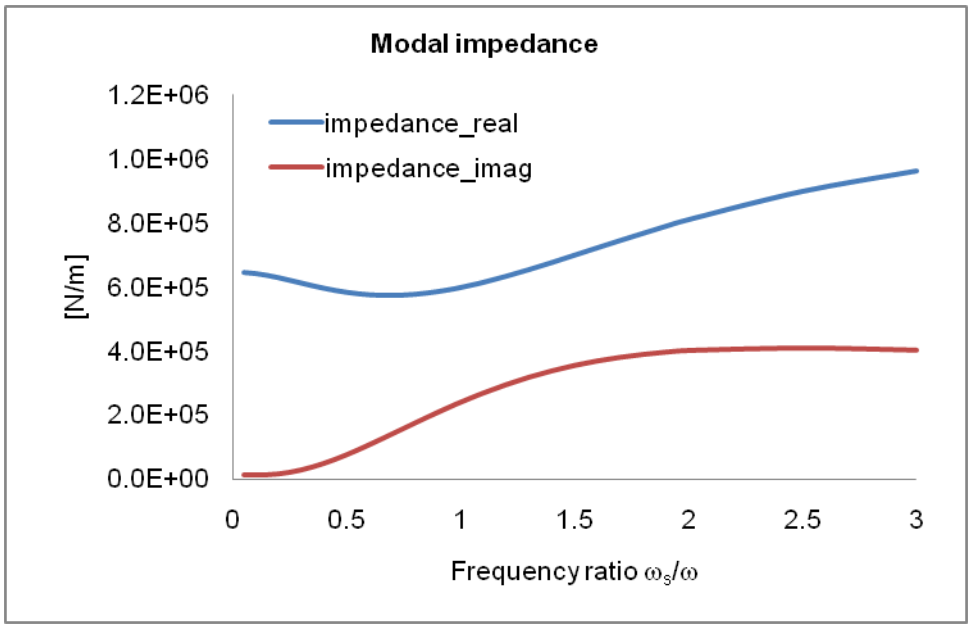

Figure 5-23 Impedance plot for original orientation

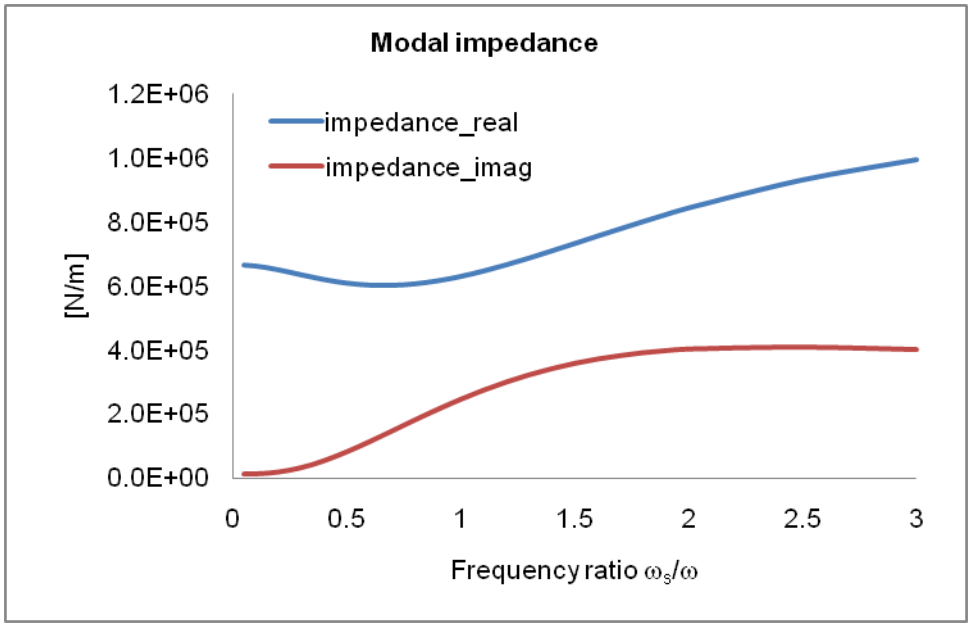

Figure 5-24 Impedance plot for 90^{o} CCW and 90^{o} CW orientation

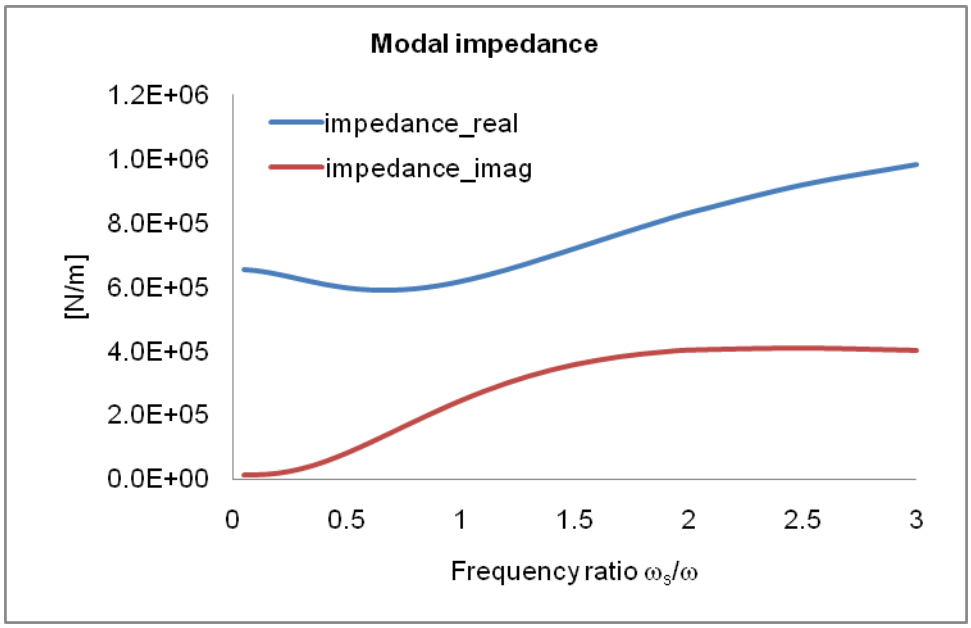

Figure 5-25 Impedance plot for 45^{o} CCW orientation

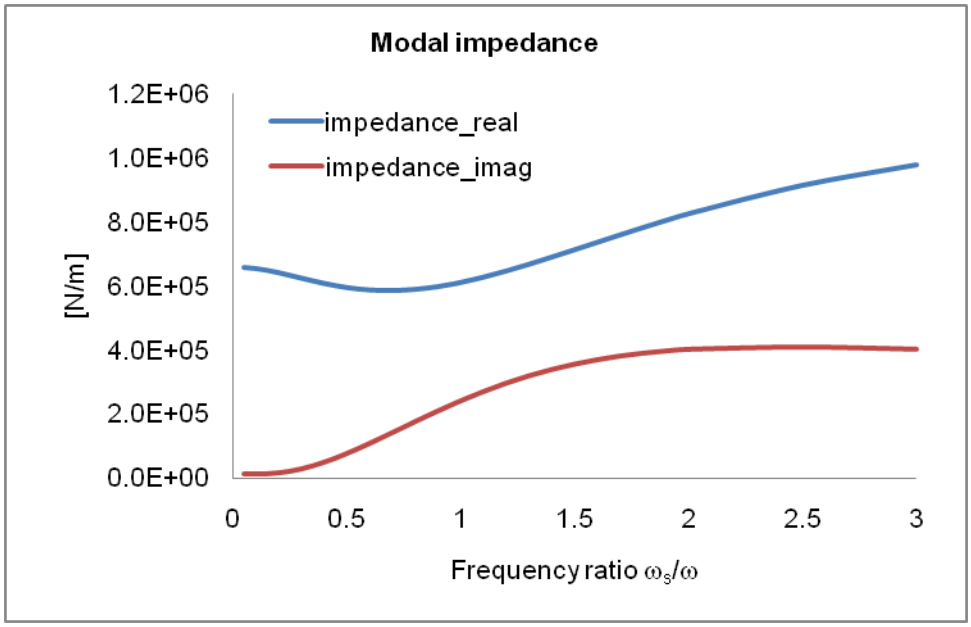

Figure 5-26 Impedance plot for 45^{o} CW orientation

Chapter 6

Conclusion and Future Work

6.1 Conclusion

Dynamic performance of the two pad offset-preloaded bearing was evaluated using the code developed by Dr. Kim. Bump stiffness and structural damping loss factor was measured using load-deflection test and hysteresis damping energy. Load-deflection tests were performed on a circular bearing with zero clearance. Hysteresis plot obtained from load-deflection test was used to determine the structural stiffness and damping loss factor of the bearing. Using the structural characteristics of the zero clearance bearing, single bump stiffness formula was derived. The bump stiffness k_{bump} of the bump foil was found to be about 8.95e5 N/m. Additionally, area enclosed in hysteresis loop was used to calculate the damping loss factor, which was about 0.134.

Optimum clearance and preload of the bearing were found. For this purpose, set of simulations were performed with different combinations of preload and hot assembly clearance. Experimentally-calculated bump stiffness and structural damping loss factor were used as input parameters to the simulation. From these simulations it was evaluated that the bearing with preload around ~ 49 μm is stable and does not have any unstable eigenmodes. Based on this, the bearing preload of 50 μm and hot assembly clearance of 63 μm was selected for the bearing.

Using designed preload and clearance, simulations were performed to check the bearing performance at different clocked orientations with respect to the loading direction. Along with the original or designed orientation bearing performance was evaluated at 90^o CCW, 90^o CW, and 45^o CCW and 45^o CW orientation. From the simulations it was found that irrespective of bearing orientation all the direct force coefficients are higher than the

cross-coupled force coefficients, indicating stability of the bearing. Furthermore, absence of eigenmode or negative imaginary impedance confirms the bearing stability. This novel feature of bearing stability at any orientation indicates that the actual micro gas turbine can be fitted in any orientation.

6.2 Future Work

This thesis presents the simulation results for force coefficients and stability analysis of the rotor. Validating the force coefficients by using external excitation source like magnetic shaker or impact hammer may be included in future work. Along with that rotordynamic analysis or imbalance response of the rotor may be included in future work.

The scope of this thesis was limited to cylindrical modal analysis due to sponsor requirement for disclosure of confidential information. Future work may include more rigorous analysis including conical mode and under various external disturbances including impeller aerodynamic forces and super-synchronous excitations.

Appendix A

Data Acquisition Using Lab View

LabVIEW VI is constructed for the data acquisition. The voltage readings for proximity sensor and load cell are show in first two chart windows. These raw voltage readings are then converted into physical displacement and loads using the calibrated plot. Chart window three and four displays actual displacement of the bearing sleeve and applied load.

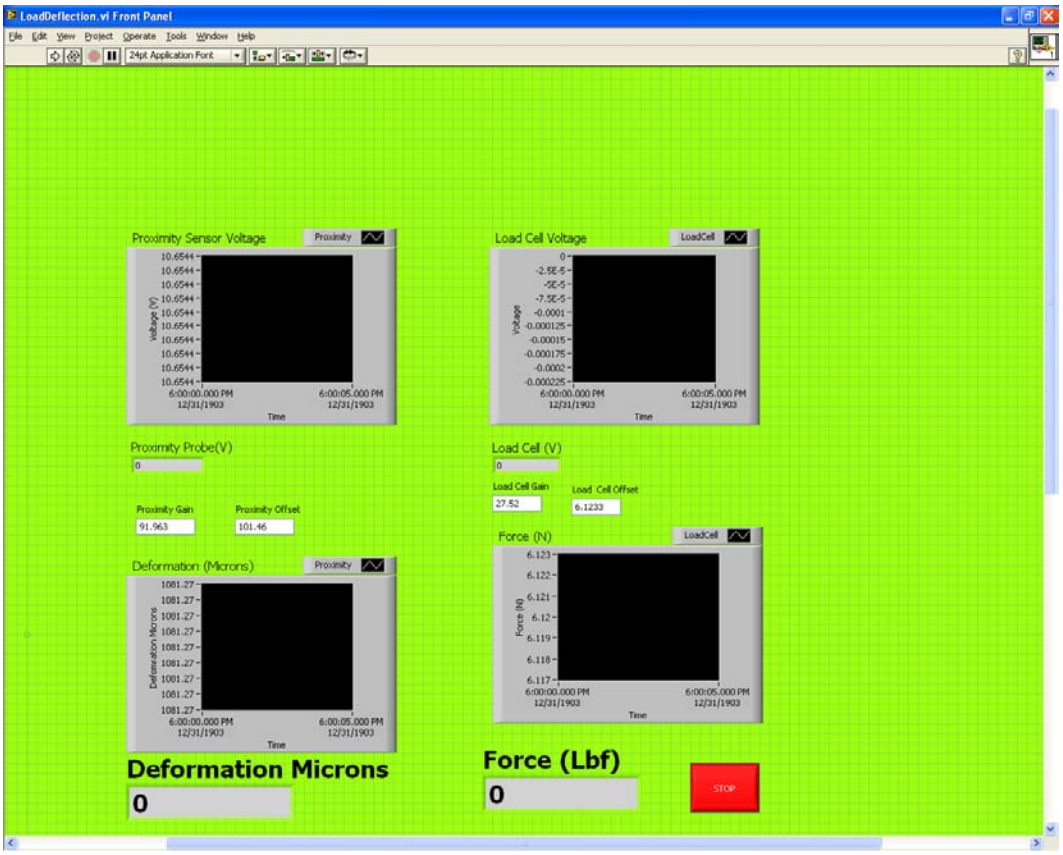

Figure A-0-1 LabVIEW VI Front Panel View

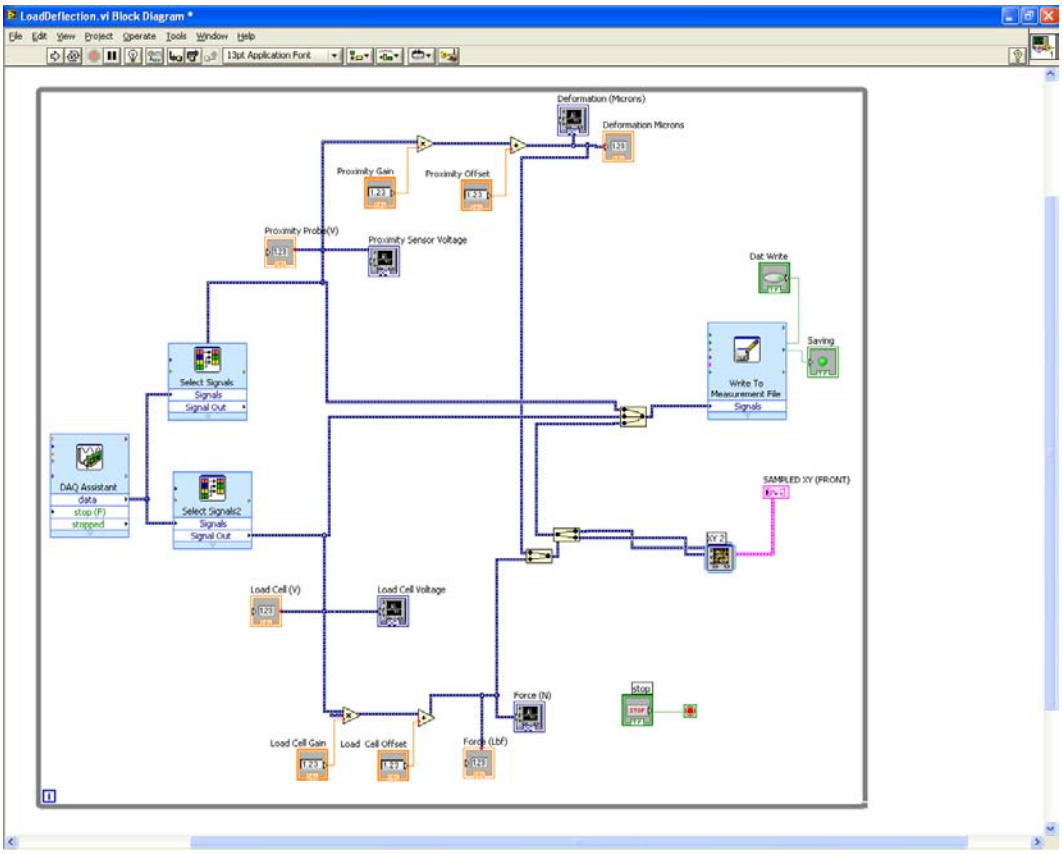

Figure A-0-2 LabVIEW VI block diagram

Bibliography

[1] Agrawal, G. L., 1997, "Foil Air/Gas Bearing Technology -- an Overview," International Gas Turbine & Aeroengine Congress & Exhibition, Orlando, FL, June 2-June 5,1997, ASME Paper No. 97-GT-347.

[2] Dykas, B., Bruckner, R., DellaCorte, C., Edmonds, B., and Prahl, J., 2008, "Design, Fabrication, and Performance of Foil Gas Thrust Bearings for Microturbomachinery Applications," ASME Turbo Expo 2008, Berlin, Germany, June 9-13, ASME Paper number GT2008-50377.

[3] Ki, J., Kim, D., and Honavara-Prasad, S., 2012, "Dynamic Modeling of a Compact Heat Exchange Reformer for High TemperatureFuel Cell Systems," Journal of Fuel Cell Science and Technology**, 9**, pp. 011013-01-16.

[4] Heshmat, H., Walowit, J. A., and Pinkus, O., 1983, "Analysis of Gas Lubricated Compliant Thrust Bearings," ASME Journal of Lubrication Technology**, 105**(4), pp. 638-646.

[5] DellaCorte, C., and Valco, M. J., 2000, "Load Capacity Estimation of Foil Air Journal Bearings for Oil-Free Turbo-Machinery Applications," STLE Tribology Transaction**, 43**(4), pp. 795-801.

[6] Iordanoff, I., 1999, "Analysis of an Aerodynamic Compliant Foil Thrust Bearing: Method for a Rapid Design," Journal of Tribology**, 121**(4), pp. 816-822.

[7] Radil, K., Howard, S., and Dykas, B., 2002, "The Role of Radial Clearance on the Performance of Foil Air Bearings," STLE Tribology Transaction**, 45**(4), pp. 485-490.

[8] Ku, C. P., and Heshmat, H., 1994, "Structural Stiffness and Coulomb Damping in Compliant Foil Journal Bearing: Parametric Studies," STLE Tribology Transaction**, 37**(3), pp. 455-462.

[9] Rubio, D., and San Andrés, L., 2006, "Bump-Type Foil Bearing Structural Stiffness: Experiments and Predictions," Journal of Engineering for Gas Turbines and Power**, 128**(3), pp. 653-660.

[10] Kim, D., 2007, "Parametric Studies on Static and Dynamic Performance of Air Foil Bearings with Different Top Foil Geometries and Bump Stiffness Distributions," ASME Journal of Tribology**, 129**(2), pp. 354-364.

[11] Song, J., and Kim, D., 2007, "Foil Gas Bearing with Compression Springs: Analyses and Experiments," ASME Journal of Tribology**, 129**(3), pp. 628-639.

[12] Lee, Y., Kim, C. H., Kim, T. H., and Kim, T. Y., 2012, "Effects of Mesh Density on Static Load Performance of Metal Mesh Gas Foil Bearings," Journal of Engineering for Gas Turbines and Power**, 134**(1), pp. 012502.

[13] Radil, K., and Zeszotek, M., 2004, "An Experimental Investigation into the Temperature Profile of a Compliant Foil Air Bearing," STLE Tribology Transactions**, 47**(4), pp. 470-479.

[14] Lee, D., and Kim, D., 2010, "Thermo-Hydrodynamic Analyses of Bump Air Foil Bearings with Detailed Thermal Model of Foil Structures and Rotor," ASME Journal of Tribology**, 132**(2), pp. 021704 (12 pages).

[15] Kim, D., 2012, *Foil bearings with multiple pads with controlled assembly clearance*, Disclosed to Office of Intellectual Property, University of Texas at Arlington.

Biographical Information

Shrikant Ashok Yadav graduated in May 2007 with Bachelors in Mechanical Engineering from University of Pune. He worked for 3 years as Senior Systems Engineer in Infosys ltd. India, developing software for 787 support data delivery project. After working as software engineer he came to UTA in fall 2010 to pursue M.S. in Mechanical Engineering.